

Polarized anisotropic spectral distortions of the CMB: Galactic and extragalactic constraints on photon-axion conversion

Suvodip Mukherjee,^{a,b,c} Rishi Khatri^d and Benjamin D. Wandelt^{a,b,c,e}

^aCenter for Computational Astrophysics, Flatiron Institute, 162 5th Avenue, 10010, New York, NY, USA

^bInstitut d'Astrophysique de Paris
98bis Boulevard Arago, 75014 Paris, France

^cSorbonne Universités, Institut Lagrange de Paris
98 bis Boulevard Arago, 75014 Paris, France

^dTata Institute of Fundamental Research
Homi Bhabha Road, Mumbai, 400005, India

^eDepartments of Physics and Astronomy, University of Illinois at Urbana-Champaign, 1002 W Green St, Urbana, IL 61801, USA

E-mail: smukherjee@flatironinstitute.org, khatri@theory.tifr.res.in, wandelt@iap.fr

Abstract. We revisit the cosmological constraints on resonant and non-resonant conversion of photons to axions in the cosmological magnetic fields. We find that the constraints on photon-axion coupling and primordial magnetic fields are much weaker than previously claimed for low mass axion like particles with masses $m_a \lesssim 5 \times 10^{-13}$ eV. In particular we find that the axion mass range 10^{-14} eV $\leq m_a \leq 5 \times 10^{-13}$ eV is not excluded by the CMB data contrary to the previous claims. We also examine the photon-axion conversion in the Galactic magnetic fields. Resonant conversion in the large scale coherent Galactic magnetic field results in 100% polarized anisotropic spectral distortions of the CMB for the mass range 10^{-13} eV $\lesssim m_a \lesssim 10^{-11}$ eV. The polarization pattern traces the transverse to line of sight component of the Galactic magnetic field while both the anisotropy in the Galactic magnetic field and electron distribution imprint a characteristic anisotropy pattern in the spectral distortion. Our results apply to scalar as well as pseudoscalar particles. For conversion to scalar particles, the polarization is rotated by 90° allowing us to distinguish them from the pseudoscalars. For $m_a \lesssim 10^{-14}$ eV we have non-resonant conversion in the small scale turbulent magnetic field of the Galaxy resulting in anisotropic but unpolarized spectral distortion in the CMB. These unique signatures are potential discriminants against the isotropic and non-polarized signals such as primary CMB, and μ and y distortions with the anisotropic nature making it accessible to experiments with only relative calibration like Planck, LiteBIRD, and CORE. We forecast for PIXIE as well as for these experiments using Fisher matrix formalism.

Keywords: Axions, Cosmic Microwave Background, Spectral Distortions

Contents

1	Introduction	1
2	Review of CMB-ALP conversion physics and current constraints from cosmology	3
2.1	Cosmological constraints: resonant case	8
2.2	Cosmological constraints: non-resonant case	11
3	Photon-ALP conversion in the Milky Way halo: Resonant case	12
3.1	Distinguishing between scalars and pseudoscalars using polarization	14
4	Photon-ALP conversion in the Milky Way halo: Non-resonant case	14
4.1	Coherent magnetic fields and electron distribution	15
4.2	Random magnetic field and turbulent gas	16
5	Forecasts for CORE, LiteBIRD and PIXIE	17
5.1	Future constraints from the unpolarized axion distortion (non-resonant conversion)	19
5.2	Future constraints from the polarized anisotropic axion distortion (resonant conversion)	20
5.3	Comparison with other experiments	23
6	Conclusions	24
A	Galactic magnetic field and electron density model	26

1 Introduction

The Cosmic Microwave Background (CMB) was discovered by Penzias & Wilson [1] and later found to have an almost perfect blackbody spectrum by Far Infrared Absolute Spectrophotometer (FIRAS) experiment [2–5] with temperature 2.7255 K (almost simultaneously confirmed by the rocket based experiment COBRA [6] with slightly less sensitivity.) Another instrument on board COBE, the differential microwave radiometer (DMR), discovered the nearly statistically isotropic fluctuations of order $10^{-5} - 10^{-4}$ K on top of the 2.7K background. The exquisite measurements of the CMB temperature and polarization angular fluctuations over the past few decades by several space-based (COBE [7], WMAP [8] and Planck [9]), ground-based (SPT [10], ACT [11], BICEP-KECK [12], POLARBEAR [13] etc.) and balloon-based (BOOMERANG [14], MAXIMA [15], etc.) missions are well explained by the 6 parameter Λ CDM (Lambda Cold Dark Matter) model and is one of the fundamental pillars of the standard cosmological model. Along with the angular fluctuations of the CMB field, we also expect deviations from the blackbody spectrum within the standard cosmological scenario [16–26] and measurement of these would deepen our understanding of both early and late time epoch of the Universe. Only one type of spectral distortion, the Sunyaev-Zeldovich effect or the y -type distortion [16], has so far been detected towards the clusters of galaxies [27–32]. Spectral distortions in CMB are also predicted by several high energy

physics scenarios which are important particularly in the pre-recombination epoch [33–39]. In brief, CMB spectral distortions provide an unexplored and extremely rich window to several astrophysical and cosmological phenomenon.

The current best constraints on the deviation of the sky-averaged CMB (monopole) from a blackbody spectrum come from FIRAS [2, 4] which gave an upper bound on spectral distortions of $\Delta I_\nu/I_\nu \lesssim 5 \times 10^{-5}$ at the peak of the blackbody spectrum. Recently, the constraints on the anisotropic spectral distortions, including the fluctuating contribution to the all sky average y -distortion were obtained from the Planck and SPT data in [40, 41]. Upcoming proposed CMB missions like PIXIE [42] would have an instrumental noise of nearly 3 – 4 orders of magnitude better than FIRAS and hence would be able to measure the CMB spectral distortions with an unprecedented accuracy [43]. Measurement of the spectral distortions signal will also depend upon the successful cleaning of the foreground contaminations [41, 44–47]. Other CMB missions like CORE[48] and LiteBIRD [49] would be able to measure the spatially fluctuating part of the spectral distortions [50] at a much better precision compared to Planck. These experiments would be polarization sensitive in all frequency channels. These missions could pioneer a new era in cosmology by measuring several guaranteed but unexplored cosmological imprints on the CMB spectrum. Along with several well known sources of spectral distortions (such as μ [17, 18, 22], y [19, 22, 25], dark matter annihilation [18]), coupling between photons and pseudoscalar axion like particles (ALPs) or light scalar particles (LSPs) in the presence of external magnetic field [51–58] is also a potential source of spectral distortion. ALPs are one of the promising candidates for dark matter and may be a solution to some of the anomalies in the standard Λ CDM model [59–64]. Regardless of whether the ALPs form the bulk of the dark matter, they are predicted almost ubiquitously in many beyond standard model theories of particle physics, including the string theory [65–67]. Indirect astrophysical searches of ALPs along with the growing ground-based experimental efforts [see 68, for a review of ground based experiments] like CAST [69], ALPS-II [70], MADMAX [71], ADMX [72], CASPER [73] are therefore very important.

The magnetic field is present in the Universe at different scales with a varying strength. The extragalactic magnetic field is expected to be of the order of 10^{-9} Gauss (nG) or smaller [74]. The extragalactic magnetic fields, particularly in voids and in the early Universe, if primordial in origin, must be stochastic (Gaussian random fields), described by a power spectrum (possibly scale invariant) [75], and therefore without a single coherence scale. Previous studies [57, 58] have considered Mpc scale extragalactic magnetic fields to study the imprints of the photon-ALP or photon-LSP conversion on CMB photons. The magnetic field is however known to be present at the Galactic (kiloparsec) scales (kpc scales), compared to only upper limits on the primordial intergalactic magnetic fields [76], with much better understanding of its strength and morphology [77, 78].

In this paper, we focus on an unexplored scenario concerning the spectral distortions of CMB photons due to photon-ALP or photon LSP conversion in the presence of the local magnetic field from Milky Way. We will consider the ALPs from now on for definiteness but our results are applicable to LSPs also in a straightforward way as explained in Sec. 3.1. The CMB photons passing through the Galactic halo to reach the earth can get converted to ALPs in the presence of the 10^{-6} Gauss (μG) magnetic field depending upon photon-ALP coupling $g_{\gamma a}$, ALP mass m_a , electron (n_e) and neutral hydrogen (n_H) number densities and strength of the magnetic field. As the Galactic magnetic field is not isotropic but exhibits large scale coherent structure and small-scale turbulent fluctuations [77–80], the spectral

distortions induced by the photon-ALP conversion must also exhibit large scale anisotropy and should be correlated with the large scale structure in the Galactic magnetic field. In particular, the regions of the sky with the stronger magnetic field can convert photons to ALPs more efficiently and than the parts of the sky with the weaker magnetic field. Secondly, the presence of fluctuations in the spectral distortion makes this phenomenon measurable from CMB missions like Planck and LiteBIRD which have only relative calibration. The spectral distortion signal from the photon-ALP conversion exhibits a unique structure in both frequency and spatial domain, which makes it easier to distinguish from other cosmological (or astrophysical) sources and other systematics.

We review the physics of photon-axion conversion and re-evaluate the existing cosmological constraints on photon-ALP conversion in section 2. We discuss the signatures of spectral distortion due to photon-ALP conversion in the Milky Way in Secs. 3 and 4 and forecast the measurability of this phenomenon from several CMB missions like Planck, PIXIE, LiteBIRD, and CoRE in Sec. 5 using Fisher Matrix. Finally in Sec. 6, we conclude our study and discuss its future implications. We use natural units (with reduced Planck constant, speed of light and Boltzmann constant respectively set to unity $\hbar = c = k_B = 1$) when discussing physics but restore physical constants when discussing observations.

2 Review of CMB-ALP conversion physics and current constraints from cosmology

Photon-ALP conversion and its cosmological consequences are well studied topics in the literature [52–55, 81–90]. ALPs and photons oscillate into each other in the presence of a magnetic field [52–55, 57]. The interaction is given by

$$\mathcal{L}_{\text{int}} = g_{\gamma a} \mathbf{E}_\gamma \cdot \mathbf{B}_{\text{ext}} a, \quad (2.1)$$

where \mathbf{B}_{ext} is the external magnetic field, \mathbf{E}_γ is the electric field of the photon, a is the axion field and $g_{\gamma a}$ is the photon-ALP coupling. Thus only the polarization with its electric field aligned with external magnetic field couples to the axion. Obviously photons and axions will couple only if the magnetic field has a component $\mathbf{B}_T = \mathbf{B}_{\text{ext}} - (\mathbf{B}_{\text{ext}} \cdot \hat{\mathbf{k}}) \hat{\mathbf{k}}$ transverse to the photon propagation direction $\hat{\mathbf{k}}$. The evolution equation for the two state quantum system, assuming relativistic ALP, is given by [53, 56]

$$\left(\omega + \begin{pmatrix} \Delta_e & \Delta_{\gamma a} \\ \Delta_{\gamma a} & \Delta_a \end{pmatrix} + i\partial_z \right) \begin{pmatrix} A_{\parallel} \\ a \end{pmatrix} = 0 \quad (2.2)$$

Here we want to study the evolution of the system along a spatial direction z , ω is the temporal frequency, in Fourier space $i\partial_z \rightarrow k$ the spatial frequency or the momentum and A_{\parallel} is the photon polarization that is parallel to the component of the magnetic field \mathbf{B}_T transverse to the propagation direction. The mixing matrix elements are defined below. In general Δ_e , which is a function of free electron, atomic and molecular densities, will vary along the photon geodesic as CMB photons travel cosmological distances. $\Delta_{\gamma a}$ is a function of magnetic field which is also spatially varying. We will, at first, ignore these complications and look at the solutions in the presence of homogeneous medium and magnetic fields and return to the inhomogeneous case later. The equation 2.2 is solved by diagonalizing the 2×2 matrix on the left hand side through rotation by mixing angle θ . The probability of conversion of a photon (with linear polarization parallel to the component of magnetic field

transverse to the propagation direction) to an ALP is then given in the homogeneous case by [57]

$$P(\gamma \rightarrow a) = \frac{(\Delta_{\gamma a} s)^2}{(\Delta_{\text{osc}} s/2)^2} \sin^2(\Delta_{\text{osc}} s/2) \equiv \sin^2(2\theta) \sin^2(\Delta_{\text{osc}} s/2) \quad (2.3)$$

where B_T is the transverse (to photon momentum) component of the magnetic field, s is the distance travelled by the photons, θ is the mixing angle defined so that $2\theta \rightarrow 0$ at high electron densities,

$$\cos(2\theta) = \frac{\Delta_a - \Delta_e}{\Delta_{\text{osc}}} \quad (2.4)$$

$$\Delta_{\text{osc}}^2 = (\Delta_a - \Delta_e)^2 + 4\Delta_{\gamma a}^2, \quad (2.5)$$

,

$$\Delta_e \equiv (n - 1)\omega, \quad (2.6)$$

and n is the refractive index for photon propagation through matter. As we see below, for high electron densities photon has real effective mass, $\Delta_e \propto -m_\gamma^2 < 0$ and $\Delta_a \propto -m_a^2 < 0$ and in the limit $|\Delta_e| \gg |\Delta_a|, |\Delta_{\gamma a}|$ mixing is suppressed ($\sin 2\theta \rightarrow 0$) and we get $\cos(2\theta) \rightarrow 1$. Similarly in vacuum, when $\Delta_e \rightarrow 0, |\Delta_a| \gg |\Delta_{\gamma a}|$, again the mixing is suppressed ($\sin 2\theta \rightarrow 0$) but we have $\cos 2\theta \rightarrow -1$. Photon axion mixing is maximum at resonance, $\Delta_e = \Delta_a$ giving $2\theta = \pi/2, \sin 2\theta = 1$.

For astrophysical matter densities, $|n - 1| \ll 1$ and can be approximated (away from resonance frequencies ω_i of atoms) by [91]

$$n - 1 \approx \frac{-m_\gamma^2}{2\omega^2} \approx \frac{2\pi\alpha}{m_e\omega^2} \left(-n_e + n_H \sum_i \frac{f_i^H \omega^2}{H\omega_i^2 - \omega^2} + n_{\text{He}} \sum_i \frac{f_i^{\text{He}} \omega^2}{\text{He}\omega_i^2 - \omega^2} \right), \quad (2.7)$$

where m_γ is the effective mass of the photon, α is the fine structure constant, ω is the angular frequency, n_e, n_H and n_{He} are the number density of free electrons, neutral hydrogen, and neutral helium respectively, f_i^α is the oscillator strength of element $\alpha \in \{H, \text{He}\}$ for transitions with energy ω_i from the ground state. For free electrons, there is no resonant frequency and the effective mass squared is positive. For neutral atoms, such as hydrogen, the effective mass squared is negative below the resonant frequency. Neutral atoms exist only after recombination and in ground state with the minimum resonant frequency of 10.2 eV corresponding to Ly- α transition of hydrogen. For CMB we will therefore always have $\omega \ll \omega_i$ and we can approximate Δ_e as (ignoring helium and heavier elements) [92]

$$\begin{aligned} \Delta_e &\approx \frac{\omega_p^2}{2\omega} \left[-1 + 7.3 \times 10^{-3} \frac{n_H}{n_e} \left(\frac{\omega}{\text{eV}} \right)^2 \right] \\ &= -2.6 \times 10^6 \left(\frac{n_e}{10^{-5} \text{cm}^{-3}} \right) \left(\frac{100 \text{ GHz}}{\nu} \right) \left[1 - 7.3 \times 10^{-3} \frac{n_H}{n_e} \left(\frac{\omega}{\text{eV}} \right)^2 \right] \text{Mpc}^{-1} \end{aligned} \quad (2.8)$$

where $\omega_p^2 = 4\pi\alpha n_e/(m_e)$ is the plasma frequency.

For the range of parameters of interest we also have

$$\Delta_{\gamma a} \equiv \frac{g_{\gamma a} |B_T|}{2} = 15.2 \left(\frac{g_{\gamma a}}{10^{-11} \text{GeV}^{-1}} \right) \left(\frac{B_T}{\mu\text{G}} \right) \text{Mpc}^{-1}, \quad (2.9)$$

$$\Delta_a \equiv -\frac{m_a^2}{2\omega} = -1.9 \times 10^4 \left(\frac{m_a}{10^{-14} \text{eV}} \right) \left(\frac{100 \text{ GHz}}{\nu} \right) \text{Mpc}^{-1} \quad (2.10)$$

$g_{\gamma a}$ is the photon-ALP coupling and $\omega = 2\pi\nu$. The photon polarization state orthogonal to B_T is unaffected. Thus initially unpolarized light propagating through a magnetic field will become polarized as intensity in one of the linear polarizations is decreased due to photon-ALP oscillation. These results apply only if both the electron density and the magnetic field are homogeneous. The departure from BlackBody (BB) spectrum for the affected polarization can be quantified by

$$\mathcal{I}^{\gamma a} = \frac{\Delta I_{\nu}^{\gamma a}}{I_{\nu}} \equiv \frac{I_{\nu}^{\text{obs}} - I_{\nu}}{I_{\nu}} = -\bar{P}(\gamma \rightarrow a), \quad (2.11)$$

where, $I_{\nu} = (h\nu^3/c^2) / (e^{h\nu/k_B T_{\text{CMB}}} - 1)$ is the Planck spectral form for single polarization in physical units, h is the Planck's constant, c is the speed of light and k_B is Boltzmann constant. This is plotted in Fig. 1a. We see that it is a fast oscillating function of frequency (as well as distance s) due to the second factor in Eq. 2.3. In any experiment with reasonable frequency and angular resolution we will only detect the result of average over many oscillations. We can therefore replace the oscillating factor with its average over an oscillation giving

$$P(\gamma \rightarrow a) = \frac{2\Delta_{\gamma a}^2}{\Delta_e^2}, \quad (2.12)$$

if the magnetic field is nearly coherent over the scales of size $s \gg \ell_{\text{osc}} \equiv 2\pi/\Delta_{\text{osc}}$. The oscillation length, ℓ_{osc} is plotted in Fig. 1b as a function of frequency ν .

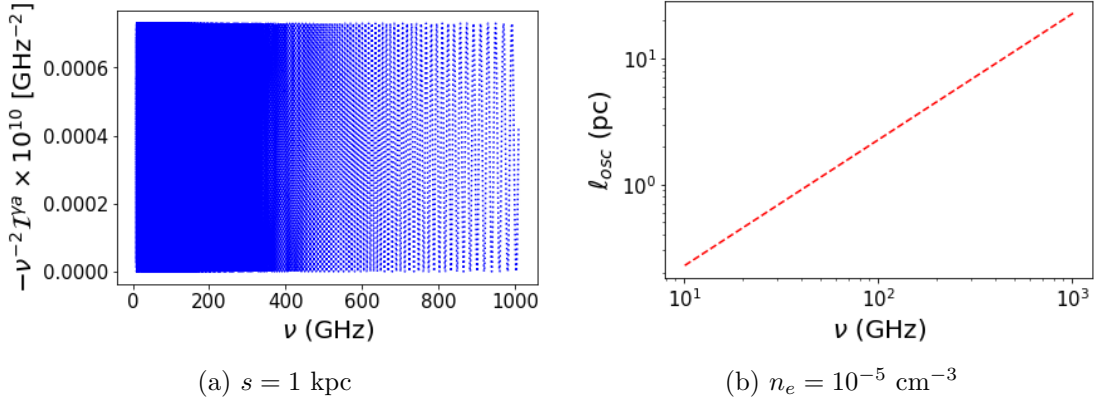


Figure 1: The left panel shows frequency dependence of the CMB spectral distortion with $n_e = 10^{-5} \text{cm}^{-3}$ and $g_{10} B_{\mu\text{G}} = 1$. The right panel shows oscillation length ℓ_{osc} as a function of photon frequency for same parameters. The axion mass is assumed to be small compared to the effective photon mass.

In reality both the electron density and magnetic fields are inhomogeneous. In particular the primordial magnetic fields (because of stochastic initial conditions) as well as small scale Galactic magnetic fields (because of turbulence) are expected to be stochastic. In this case,

as a toy model, we can approximate the magnetic fields as composed of independent domains of size d_0 such that the magnetic field and electron density are homogeneous inside each domain but in different domains the magnetic field has different random orientations but same strength for simplicity. In the limit of large number of domains we can obtain an analytical solution for the conversion probability of the total unpolarized intensity given by [57, 93]

$$\bar{P}(\gamma \rightarrow a)(r) = \frac{1}{3} \left(1 - e^{(-3P(\gamma \rightarrow a)r/2d_0)} \right) \quad r \gg d_0, \quad (2.13)$$

where r is the size of the turbulent region, $P(\gamma \rightarrow a)$ is the probability of conversion inside each domain and \bar{P} is the average conversion probability over the whole turbulent region. In this case, we have a spectral distortion but no polarization. In the limit $r \rightarrow \infty$ we saturate the probability with $1/3^{\text{rd}}$ of the photons getting converted into ALPs.

The true situation will be in between the above two extreme limits and both the magnetic field and electron density would vary along the photon geodesic. In particular, when photons and ALPs propagate through the inhomogeneous medium, there is the possibility of resonance when the effective mass of photon becomes equal to the mass of the ALP,

$$\Delta_e = \Delta_a. \quad (2.14)$$

For inhomogeneous matter distribution and magnetic fields, relevant for considering the CMB - ALP conversions, the conversion probability is sensitive to how fast the matter/electron density and the magnetic fields, and therefore the mixing angle 2θ , change compared to the oscillation length, $\ell_{\text{osc}} = 2\pi/\Delta_{\text{osc}}$ [56]. We therefore define an adiabaticity parameter (with ∇ denoting the spatial derivative with respect to the physical distance along the line of sight or proper time),

$$\begin{aligned} \gamma_{\text{ad}} &= \left| \frac{\pi}{\ell_{\text{osc}} \nabla \theta} \right| \\ &= \left| \frac{\Delta_{\text{osc}}}{\sin(2\theta) \cos(2\theta) \nabla(\ln \Delta_{\gamma_a}) + \sin(2\theta) \Delta_e / \Delta_{\text{osc}} \nabla(\ln \Delta_e)} \right| \end{aligned} \quad (2.15)$$

with the adiabatic limit defined as $\gamma_{\text{ad}} \gg 1$. The propagation is adiabatic when the length scale over which the mixing angle changes, $1/\nabla\theta$ is much larger than the oscillation length ℓ_{osc} . In the adiabatic limit, the final conversion probability depends only on the initial mixing angle when the photon is emitted, θ_0 , and the final mixing angle at the detector θ irrespective of whether there is a resonance [56]

$$P(\gamma \rightarrow a) = \frac{1}{2} (1 - \cos 2\theta_0 \cos 2\theta) \quad (2.16)$$

The first term in the denominator in Eq. 2.15 arises due to the inhomogeneous magnetic fields and the second term due to inhomogeneity in the matter distribution and ionization fraction. At resonance $\sin(2\theta) = 1$; $\cos(2\theta) = 0$ and the first term in the denominator due to the inhomogeneous magnetic field vanishes. Therefore, for resonant conversion only the inhomogeneity in the matter is relevant and the adiabaticity parameter becomes

$$\gamma_{\text{ad}}(\text{resonance}) = \frac{4\Delta_{\gamma_a}^2}{|\nabla \Delta_e|}. \quad (2.17)$$

A given cosmological average recombination and reionization history fixes the denominator. We can therefore plot the $g_{\gamma a} B_T$ for which $\gamma_{\text{ad}}(\text{resonance}) = 1$ as a function of redshift. This curve separates the adiabatic and non-adiabatic regions of the parameter space at each redshift. For values of $g_{\gamma a} B_T$ above this curve we will have adiabatic resonances for ALP mass which satisfies $m_a = m_\gamma$ at that redshift and below this curve we will have a non-adiabatic resonance. This is shown in Fig. 2. The comoving magnetic field is plotted which is related to the physical magnetic field by $B_T(\text{physical}) = (1+z)^2 B_T(\text{comoving})$.

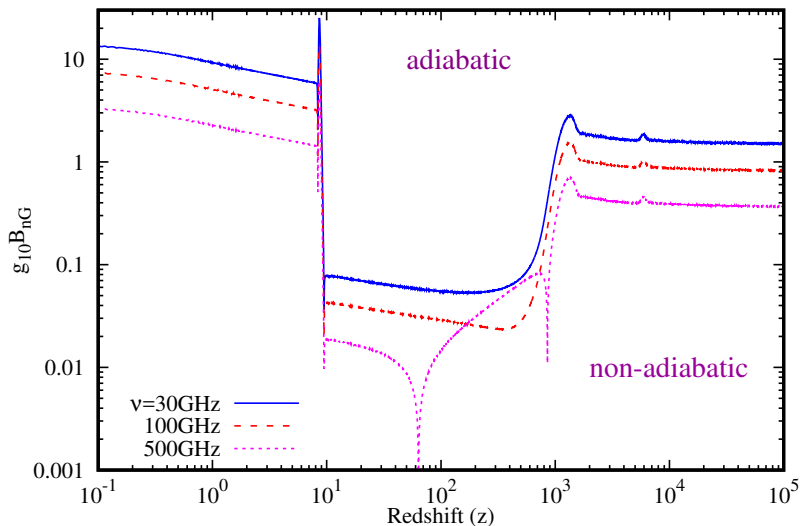


Figure 2: Transition condition between the adiabatic and non-adiabatic resonance is plotted as $g_{\gamma a} B_T(\text{comoving})$ in units of $10^{-10} \text{ GeV}^{-1} \text{ nG}$. The $g_{\gamma a} B_T$ much larger than the threshold curves will result in adiabatic resonances while much smaller values will result in non-adiabatic resonances.

For the non-trivial solutions of Eq. 2.2 to exist, the determinant of the operator on the left hand side must vanish. This gives us two dispersion relations [56] defining the two eigenstates ($m_{\text{eff}}^2 = \omega^2 - k^2 \approx 2\omega(\omega - k)$) of the system,

$$\begin{aligned}
 2\omega(\omega - k) &= -\omega(\Delta_e + \Delta_a) \pm \omega\Delta_{\text{osc}} \\
 &= \frac{m_a^2 + m_\gamma^2}{2} \pm \left[\left(\frac{m_a^2 - m_\gamma^2}{2} \right)^2 + \omega^2 g_{\gamma a}^2 B_T^2 \right]^{1/2}
 \end{aligned} \tag{2.18}$$

The dispersion relations or the eigenstates of the Hamiltonian are shown in Fig 3 as a function of the electron number density assuming fully ionized plasma. The resonance happens when $m_a = m_\gamma$. If the resonance is adiabatic, $\gamma_{\text{ad}} \gg 1$, the system stays in the instantaneous eigenstate on the same branch of the dispersion relation. In particular in this case a photon produced at high density away from the resonance would follow the upper branch as the density of the medium decreases and we will have a full conversion to ALPs at sufficiently low densities¹. This can also be seen from Eq. 2.16 with $\cos 2\theta_0 \approx 1, \cos 2\theta \approx -1$ giving $P(\gamma \rightarrow a) \approx 1$. If the density of the medium changes rapidly compared to the oscillation

¹This is similar to the MSW effect [94–96] in case of neutrino flavor oscillations

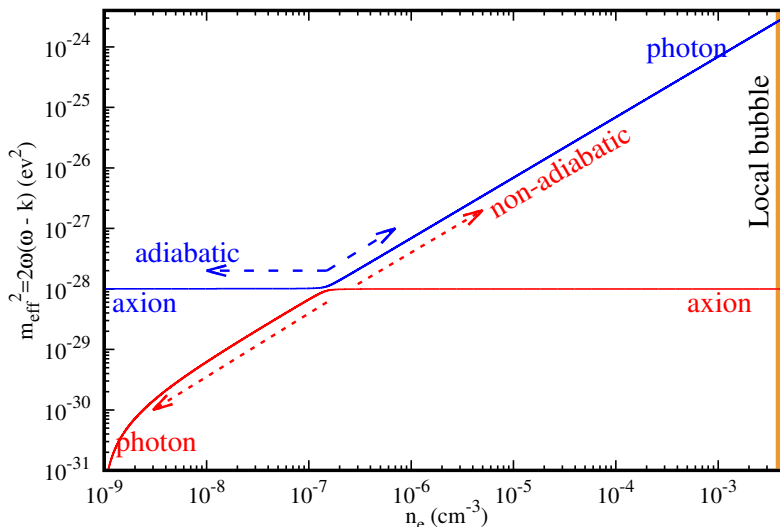


Figure 3: Dispersion relations for the photon-ALP system as a function of the electron density. The electron density in the solar neighbourhood, in particular the local bubble, is also marked. For this plot the ALP mass is $m_a = 10^{-14}$ eV, and $g_{\gamma a} B_T = 10^{-6} \text{Gev}^{-1} \text{nG}$. Also shown are the trajectories along the dispersion relations for adiabatic and non-adiabatic cases when photons/ALP are propagating through an inhomogeneous plasma.

length, ℓ_{osc} , there is a non-zero probability that the quantum system would make a transition between the two eigenstates or branches of the dispersion relation. In the limit that the change in density near the resonance is linear, the transition probability is given by the Landau-Zener formula [56, 97–100]

$$p = e^{-\pi\gamma_{\text{ad}}/2} \quad (2.19)$$

and the conversion probability is

$$P(\gamma \rightarrow a) = \frac{1}{2} (1 - (1 - 2p) \cos 2\theta_0 \cos 2\theta) \quad (2.20)$$

The cosmic evolution of the photon effective mass m_γ is shown in Fig. 4. For detection at earth, we should take into account the fact that solar system is inside a local hot bubble with electron density $\sim 5 \times 10^{-3} \text{cm}^{-3}$ [105–107] with radius ~ 100 pc. The ionization fraction is high enough that we can ignore the neutral hydrogen contribution to the photon mass, yielding $m_\gamma^{\text{local}} \approx 2.6 \times 10^{-12}$ eV. This is also shown in Fig. 4. For ALP masses far from resonance, we have the oscillation length $\ell_{\text{osc}} \lesssim 7 \times 10^{-3} (\nu/150 \text{GHz})$ pc. Therefore, for $m_a \gg m_\gamma^{\text{local}}$ we are detecting the photons in vacuum while for $m_a \ll m_\gamma^{\text{local}}$ we are detecting the photons at high electron density. Previous analysis of cosmological CMB constraints has assumed the cosmic average electron density of $n_e \approx 2 \times 10^{-7} \text{cm}^{-3}$ for calculating m_γ at the detection point [58, 108].

2.1 Cosmological constraints: resonant case

Before the epoch of electron-positron annihilation at $z \sim 10^8 - 10^9$, the high electron-positron number density results in large scattering rate of photons with electron and positrons, heavily

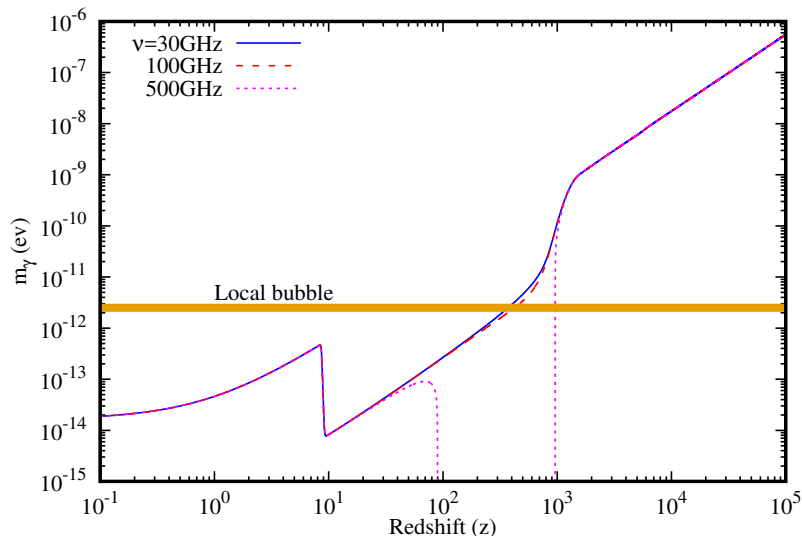


Figure 4: Cosmic evolution of the photon effective mass m_γ . We assume a standard Λ CDM recombination history with reionization happening at $z = 8$ calculated using CLASS [101] in HyREC mode [102–104].

damping the photon-ALP conversions [109, 110]. We can therefore take as the initial state pure photons at $z \sim 10^8$. Depending on the ALP mass, we may have one or more resonances between $z = 10^8$ and today. We can roughly estimate the effect of resonances on the final state from Fig. 3. As long as the resonances are non-adiabatic and the detection is done far from the resonance, the probability of conversion remains small. Also, if there are an even number of completely adiabatic resonances, we again end up with a photon. To get a large conversion probability from photon to ALP we must have an odd number of adiabatic resonances. From Fig. 4, we see that for $m_a \gtrsim 3 \times 10^{-12}$ there is only one resonance and the condition that this resonance should be non-adiabatic gives an upper limit on $g_{\gamma a} B_T$ (Fig. 2). For $8 \times 10^{-15} \lesssim m_a \lesssim 2 \times 10^{-12}$ multiple resonances happen. In this case, the most stringent constraints would come from the most adiabatic resonance which would occur between recombination and reionization from Fig. 2. These constraints have already been derived by [108] and we will not repeat them here. It was claimed in [58] that the occurrence of two non-adiabatic resonances places very stringent constraints and in particular rules out the mass range between $10^{-14} \leq m_a \leq 5 \times 10^{-13}$. However, we see from Fig. 3 that this cannot happen. In fact starting at high density and going through two non-adiabatic resonances, we will end up in the top dispersion relation in Fig. 3 on the right/high-density side of the resonance. In [58] however it was assumed that the photons are finally detected in vacuum, implying an additional adiabatic resonance which is not present in the formula (for two resonances) that they used making these constraints of [58] invalid. If there was indeed an additional adiabatic resonance, it would be this resonance which would provide the final constraint on $g_{\gamma a} B_T$ as were derived in [108].

We can make the above statements precise as follows. Let us denote the two eigenstates after a^{th} resonance (far from the resonance) plotted in Fig. 3 by normalized states $|\psi_1(a)\rangle, |\psi_2(a)\rangle$. Each of these eigenstates ψ_i is a superposition of photon and axion as determined by the mixing angle θ . The level crossing probability p then denotes the probability

of going from initial state $|\psi_i(0)\rangle$ to final state $|\psi_j(1)\rangle$ after crossing one resonance,

$$|\langle\psi_i(1)|\psi_j(0)\rangle|^2 = \begin{pmatrix} 1-p & p \\ p & 1-p \end{pmatrix}. \quad (2.21)$$

In case of N resonances we get [100, 111]

$$\begin{aligned} |\langle\psi_i(N)|\psi_j(0)\rangle|^2 &= |\langle\psi_i(N)|\cdots|\psi_k(a)\rangle\langle\psi_k(a)|\psi_l(a-1)\rangle\langle\psi_l(a-1)|\cdots|\psi_j(0)\rangle|^2 \\ &= \prod_{a=1}^N \begin{pmatrix} 1-p_a & p_a \\ p_a & 1-p_a \end{pmatrix} \equiv \begin{pmatrix} 1-p & p \\ p & 1-p \end{pmatrix}, \end{aligned} \quad (2.22)$$

where p is the final level crossing probability after N resonances which can be written as

$$p = \frac{1}{2} \left(1 - \prod_{a=1}^N (1 - 2p_a) \right). \quad (2.23)$$

In the above calculation we have ignored the interference between different resonances and treated the level crossing probabilities as classical probabilities. This is justified if there is decoherence in the wavefunction evolution [112, 113], for example, due to propagation through the stochastic primordial magnetic fields in-between the resonances. Starting at high electron densities, in case of N even, we will be back on the right side of the resonance in Fig. 3 while for N odd we will end up on the left (or low electron density) side of resonance. The photon to axion probability is equal to the probability that starting with an approximately pure photon case on the upper eigenstate at high electron densities we end up on the axion line far from the resonance. It is therefore given by

$$P(\gamma \rightarrow a) = \begin{cases} p & : N \text{ even} \\ 1-p & : N \text{ odd} \end{cases} \quad (2.24)$$

We note that we do not have a choice to independently choose N even or odd and at the same time require final detection at high density or in vacuum. Specifying one condition automatically fixes the other.

For the frequency range $\nu \gtrsim 150$ GHz, we will always have two resonances during the dark ages for small axion masses on account of the effective mass of photon getting dominated by neutral gas and becoming imaginary and then real again once reionization starts. In this case of two resonances, starting at upper left curve in Fig. 3, the conversion to axion would occur if at one of the resonances we cross level (with probability p_i) but fail to do so at the other resonance (with probability $(1-p_j)$), where p_i is the level crossing probability for i th resonance. We therefore have the total conversion probability for two resonances

$$P(\gamma \rightarrow a) = p = p_1(1-p_2) + p_2(1-p_1) \quad (2.25)$$

in agreement with Eq. 2.23 and similar situation in [58]. This result is true for all axion masses, including $10^{-14} \leq m_a \leq 5 \times 10^{-13}$. It is also clear that if one of resonances is more adiabatic than the other (larger $(1-p_i)$), then that resonance will dominate the overall probability. Using $P(\gamma \rightarrow a) = p$ (instead of $P(\gamma \rightarrow a) = 1-p$ used by [58]) for this mass range yields the correct constraint which is similar to the mass range just outside this interval and much weaker than what is claimed in [58].

2.2 Cosmological constraints: non-resonant case

For axion mass $m_a \leq 10^{-14}$ the only resonances are the ones during the dark ages when the effective mass of the photons becomes imaginary for $\nu \gtrsim 150$ GHz (observed frequency today). These constraints are considered in [58]. In this case we can also expect competitive constraints from non-resonant photon-axion oscillations in the stochastic primordial magnetic fields in voids [57]. Previous studies of non-resonant conversion have relied on the toy model of randomly oriented magnetic field domains leading to Eq. 2.13. This is however an unrealistic oversimplification. More realistically we should expect the primordial magnetic fields to be Gaussian random vector fields with a power spectrum that depends on the production mechanism [75]. In this case we cannot separate the voids into homogeneous regions across which the magnetic fields change abruptly. The variation in magnetic fields across the void would be smooth and the adiabaticity parameter, Eq. 2.15 plays an important role in this case. For the adiabatic evolution Eq. 2.16 applies and the conversion probability would be determined by the high density regions at the edge of void with small mixing angles rather than the low density regions near the center of the void with large mixing angles. For adiabatic evolution therefore we expect the photon-axion conversion to be highly suppressed.

For low axion masses, $\Delta_a \ll \Delta_e$ and small mixing angle $\Delta_{\gamma a} \ll \Delta_e$ we have $\cos 2\theta \approx 1$ and the expression for adiabaticity parameter can be simplified, taking a single Fourier mode k_B, k_e for the magnetic field and electron distribution respectively,

$$\begin{aligned} \gamma_{\text{ad}} &\approx \left| \frac{\Delta_{\text{osc}}}{\sin(2\theta) (k_B + k_e)} \right| \\ &\approx 2 \left(\frac{n_e}{10^{-9} \text{ cm}^{-3}} \right)^2 \left(\frac{10^{-10} \text{ GeV}^{-1}}{g_{\gamma a}} \right) \left(\frac{1 \text{ nG}}{B_T} \right) \left(\frac{0.1 \text{ pc}^{-1}}{k_B} \right), \end{aligned} \quad (2.26)$$

where we have assumed that the magnetic field changes more rapidly than the electron density. We also need the magnetic field to change randomly in order for Eq. 2.13 to be applicable, therefore the evolution should be non-adiabatic w.r.t the changes in the magnetic field. We see from Eq. 2.26 that we have adiabatic evolution on scales $\gg \text{pc}$, in particular for Mpc scale magnetic fields considered by [57] rendering their calculations unrealistic. Most of the contribution to $P(\gamma \rightarrow a)$ would come from magnetic fields on parsec scales or smaller where the contributions from different domains can add incoherently. We are therefore in the regime where $\Delta_{\text{osc}s} \ll 1$ in each domain of size $s \sim 10 \text{ pc}$. In this limit we get from Eqs. 2.3 and 2.13 for a void of radius R_V

$$\begin{aligned} \bar{P}(\gamma \rightarrow a) &\approx \frac{P(\gamma \rightarrow a) R_V}{2s} \\ &\approx \frac{\Delta_{\gamma a}^2 R_V s}{2} = 10^{-4} \left(\frac{g_{\gamma a}}{10^{-10} \text{ GeV}^{-1}} \right)^2 \left(\frac{B_T}{1 \text{ nG}} \right)^2 \left(\frac{R_V}{1 \text{ Gpc}} \right) \left(\frac{s}{10 \text{ pc}} \right) \end{aligned} \quad (2.27)$$

We note that in this limit the conversion probability is independent of frequency. The COBE-FIRAS limit on change in the CMB frequency spectrum at the peak of blackbody [2, 4] of $\lesssim 5 \times 10^{-5}$ translates into $g_{\gamma a} B_T \lesssim 10^{-10} \text{ GeV}^{-1} \text{ nG}$, which is a factor of ~ 20 weaker than the limits obtained in [57]. Our limit is still a very rough limit. To get precise constraints we must evolve the CMB photons through a realistic void profile with a realization of Gaussian random magnetic field which we leave for future work. We can however make the following important observations from above discussion. We see from Eq. 2.26 that smaller scales are more non-adiabatic and should therefore contribute the most to the photon-axion

conversion. However from Eq. 2.27 we see that the conversion probability decreases for small scales. The conversion probability in a domain and the effect of adiabaticity therefore oppose each other. We therefore have a sweet spot or a range of scales (around 10 pc for $g_{\gamma a} B_T = 10^{-10} \text{ GeV}^{-1} \text{ nG}$) for which the net conversion probability is maximized.

3 Photon-ALP conversion in the Milky Way halo: Resonant case

The previous work on CMB-ALP conversion only considered the cosmological evolution of the mean electron density and primordial magnetic fields. We can extend the analysis by considering the propagation of CMB photons in the local Universe through the Milky Way halo to the Solar System. On scales greater than $\sim 100 \text{ Mpc}$, we expect to approach the homogeneous Universe [115–120] and the electron density to reach the cosmic mean value of $\approx 2 \times 10^{-7} \text{ cm}^{-3}$. The electron density should increase to the Milky Way circumgalactic value of $\approx 10^{-5} \text{ cm}^{-3}$ near the Milky Way halo at radius of about $\approx 100 \text{ kpc}$ [121] to $\sim 10^{-1} \text{ cm}^{-3}$ near the plane of the Galaxy [122] before decreasing to $\sim 5 \times 10^{-3} \text{ cm}^{-3}$ in the local hot bubble surrounding the Solar system [105–107]. Of course, we do not expect the density to vary smoothly from intergalactic medium to us but expect the distribution of matter to be fractal and filamentary [123–127] and we leave a more careful and precise analysis taking into account the inhomogeneities in the electron density for future work. We can still get rough constraints using the average electron density variation from the intergalactic medium to the Solar system. At $n_e = \{2 \times 10^{-7}, 10^{-5}, 10^{-1}\} \text{ cm}^{-3}$, $m_\gamma = \{1.7 \times 10^{-14}, 1.2 \times 10^{-13}, 1.2 \times 10^{-11}\} \text{ eV}$ respectively. For $10^{-14} \lesssim m_a \lesssim 10^{-12}$ (the upper limit coming from the density in the local bubble of $n_e \sim 5 \times 10^{-3} \text{ cm}^{-3}$), there is only one resonance and we can assume production in vacuum ($\cos \theta_0 = 1$) and detection at high densities ($\cos \theta = -1$) giving the level crossing probability (Eq. 2.20)

$$P(\gamma \rightarrow a) = 1 - p \approx \frac{\pi \gamma_{\text{ad}}}{2} \approx \frac{2\pi \Delta_{\gamma a}^2}{|\nabla \Delta_e|} \lesssim 10^{-4} \quad (3.1)$$

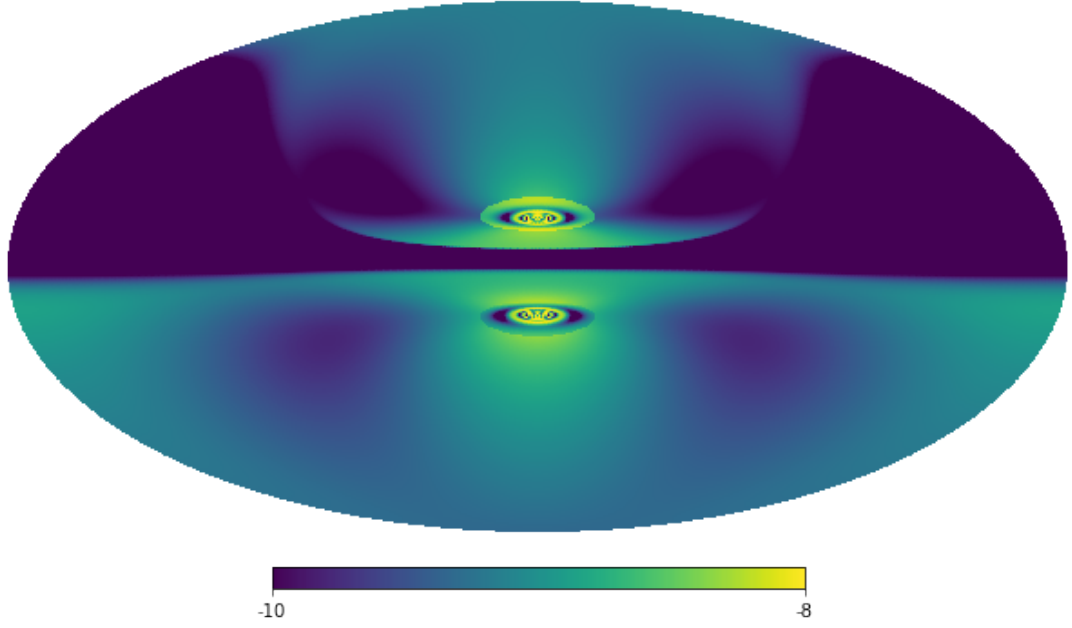
$$\Delta_{\gamma a} \lesssim \left(\frac{10^{-4} |\nabla \Delta_e|}{2\pi} \right)^{1/2}, \quad (3.2)$$

where we assumed that $p \approx 1$ to satisfy COBE constraint [2, 4] that the fractional change in CMB spectrum should be $\lesssim 10^{-4}$. For $10^{-14} \lesssim m_a \lesssim 10^{-13} \text{ eV}$, the resonance happens outside the Galactic halo with $|\nabla \Delta_e| \approx 2.5 \times 10^4 \text{ Mpc}^{-2}$ at 100 GHz and for $10^{-13} \lesssim m_a \lesssim 10^{-11} \text{ eV}$ there will be a resonance inside the Galactic halo with $|\nabla \Delta_e| \approx 2.6 \times 10^{11} \text{ Mpc}^{-2}$ at 100 GHz giving

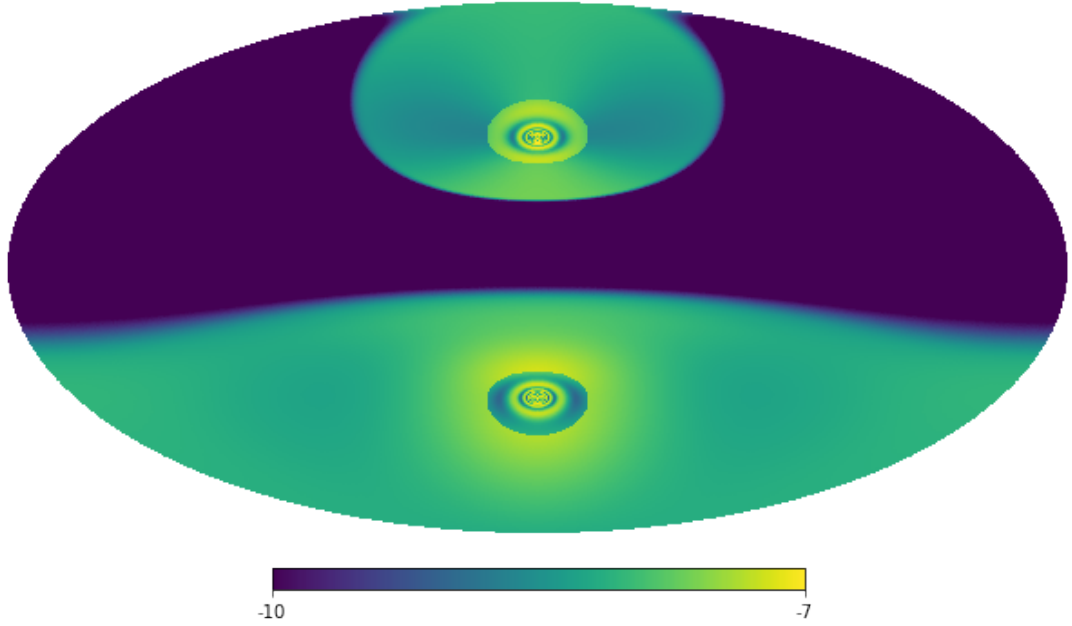
$$\begin{aligned} g_{\gamma a} B_T < 4 \times 10^{-10} \text{ GeV}^{-1} \text{ nG} & \quad | \quad 10^{-14} \lesssim m_a \lesssim 10^{-13} \text{ eV} \\ g_{\gamma a} B_T < 13 \times 10^{-10} \text{ GeV}^{-1} \mu\text{G} & \quad | \quad 10^{-13} \lesssim m_a \lesssim 10^{-11} \text{ eV} \end{aligned} \quad (3.3)$$

We should emphasize an important difference between the last constraint and the constraints we get on cosmological scales: We know that the Galactic magnetic field with strength of μG exists [77, 78]. The above constraints is therefore directly on the coupling constant $g_{\gamma a}$ where as the constraints of [108] are on the combination $g_{\gamma a} B_T$.

For $10^{-12} \lesssim m_a \lesssim 10^{-11}$ there will be a second resonance as the photons propagate from ISM to the local hot bubble surrounding the solar system which would be less adiabatic and hence give weaker constraints.



(a) For axion mass $m_a = 5 \times 10^{-12}$ eV



(b) For axion mass $m_a = 5 \times 10^{-13}$ eV

Figure 5: Maps of the resonance conversion signal from photon-ALP at photon frequency $\nu = 150$ GHz for $g_{11} = 10^{-11}$ GeV $^{-1}$ with Galactic magnetic field and electron density is depicted in \log_{10} scale in the Galactic coordinates with $n_{\text{side}}=512$ using HEALPix subroutine [114]. The signal $\Delta I_\nu/I_\nu \geq 10^{-10}$ corresponds to a sky fraction of (a) $f_{\text{sky}} = 0.68$ and the mean signal of 8.34×10^{-10} and (b) $f_{\text{sky}} = 0.41$ and the mean signal 1.06×10^{-8} for the two cases.

For the resonant conversion in the Galactic halo we can use the model of Galactic magnetic field and electron number density derived from astrophysical observations including synchrotron radiation, Faraday rotation, dispersion of pulsar radiation, angular broadening of extragalactic sources and other effects associated with scattering of radiation by electrons [77, 78, 122, 128]. The details of the Galactic model are given in Appendix A. Given a model of Galactic magnetic field and electron distribution, we can calculate the photon-to-axion resonant conversion probability for a given axion mass m_a along any direction using Eq. 3.1 at the distance r from us where $m_a = m_\gamma$. The results are shown in Fig. 5 for $m_a = 5 \times 10^{-12}, 5 \times 10^{-13}$ eV assuming $g_{\gamma a} = 10^{-11}$ GeV $^{-1}$ at observed frequency $\nu = 150$ GHz. A given axion mass traces a complicated shell around the Galaxy where $m_a = m_\gamma$ resulting in rich features in the CMB spectral distortion map. In particular, given a Galactic model, each mass m_a has its unique morphological signature in the CMB sky which is quite different from any known cosmic or Galactic foregrounds and backgrounds. The north-south asymmetry in Fig. 5 is a reflection of the north-south asymmetry in the Galactic magnetic field (see Appendix A). We should emphasize that in addition this distortion is 100% polarized and therefore can be easily distinguished from non-polarized cosmic and Galactic components. The lower axion masses come into resonance further out in the halo where the electron number density is smaller giving higher distortions.

3.1 Distinguishing between scalars and pseudoscalars using polarization

If we had new low mass scalar particles (LSPs) mixing with the photons [56], we would get a similar anisotropic distortion pattern as in the case of pseudoscalars such as ALPs. The interaction for scalars (ϕ) is given by

$$\mathcal{L}_{\text{int}} = g_{\gamma\phi} \mathbf{B}_\gamma \cdot \mathbf{B}_{\text{ext}} \phi \quad (3.4)$$

and should be compared to Eq. 2.1. In Eq. 3.4 \mathbf{B}_γ is the magnetic field of the photon and \mathbf{B}_{ext} is the external magnetic field. For the scalars therefore, in the presence of external magnetic field, the photon polarization with its magnetic field along the external magnetic field is coupled to the axions and therefore the polarization of the distortion is rotated by 90° compared to the pseudoscalars or ALPs. For equivalent couplings, we will therefore have the same anisotropy signal on the sky but orthogonal polarization. The polarized signal discussed in this section, if detected, will not only tell us whether there is a light particle that mixes with photons and the mass of this particle but also whether it is a scalar or a pseudoscalar.

4 Photon-ALP conversion in the Milky Way halo: Non-resonant case

There is no resonance for $m_a \lesssim 10^{-14}$ eV except for the resonances expected when neutral gas is encountered with very low ionization fraction [108] and we will ignore these as they require a detailed multiphase model of the Galaxy. For $m_a > 10^{-11}$ eV $^{-1}$, the required values of $g_{\gamma a}$ to produce any observable spectral distortions are ruled out by CAST [69]. We will consider non-resonant conversion for $m_a \lesssim 10^{-14}$ eV in this section.

For Milky way halo, the typical length of the coherent magnetic field is of kpc scale with the strength of μG [77, 78]. In addition, there is a turbulent component to the magnetic field in the Milky Way confined mostly in the Galactic plane with coherent lengths of 100 pc or less [129–131]. Galactic magnetic field and electron density distribution in the Galactic halo is not yet known very accurately, but the situation is expected to improve with the upcoming

missions like SKA [132] in the future. The recent measurement of the Galactic magnetic field from Faraday rotation map [79] and Planck dust map [80] also indicates fluctuations in the magnetic field dominant at large angular scales. As a result, we can also expect large-scale fluctuations in the component of Galactic magnetic field transverse to the direction of propagation. For the purpose of photon-axion conversion, what is important is not the fluctuations in electron density but rather the fluctuations in photon effective mass which can transition from real to being imaginary in the highly neutral gas. Fluctuations in the electron ionization fraction can thus make the propagation of photons/axions highly non-adiabatic and should be important for non-resonant conversion.

4.1 Coherent magnetic fields and electron distribution

A model of the coherent component of the Galactic magnetic field in the disk and halo of Milky way was developed by Jansson et al. [78]. The Magnetic field in the Galactic halo can be written as a superposition of a toroidal and poloidal components. In both these components the magnetic field changes on scales of \sim kpc (see Appendix A for details).

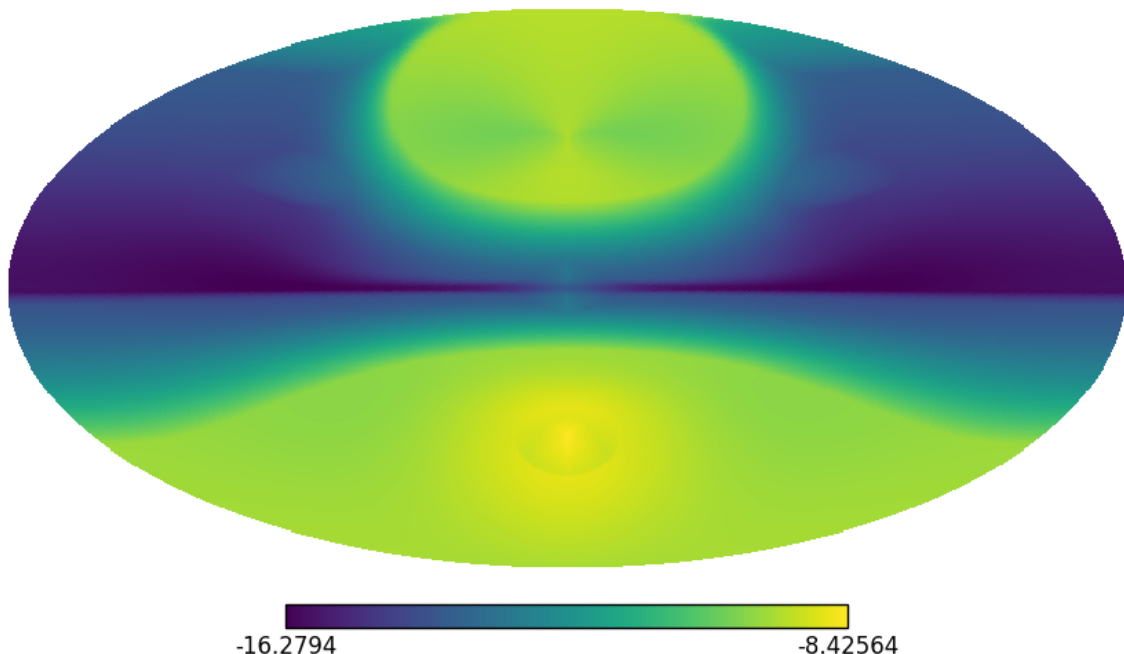


Figure 6: A map of the maximum probability of conversion from photon-ALP at photon frequency $\nu = 500$ GHz in the Galactic coordinates with $n_{\text{side}}=1024$ using HEALPix subroutine [114] are depicted in \log_{10} scale

The electron density also decreases exponentially with increasing distance from the Galactic plane [121, 122, 128] with a scale height again of order \sim kpc. The photon-ALPs conversion probability, Eq. 2.3, is proportional to B_T^2/n_e^2 for $m_a \lesssim 10^{-14}$ eV. Since both B_T and n_e decrease with increasing distance from the Galactic center and the Galactic plane, there will be a maximum conversion probability at some distance s for each direction in the sky and hence we can have a map of this effect. This map provides an upper limit to the axion spectral distortion we can expect in the CMB. Using the model of the Galactic magnetic

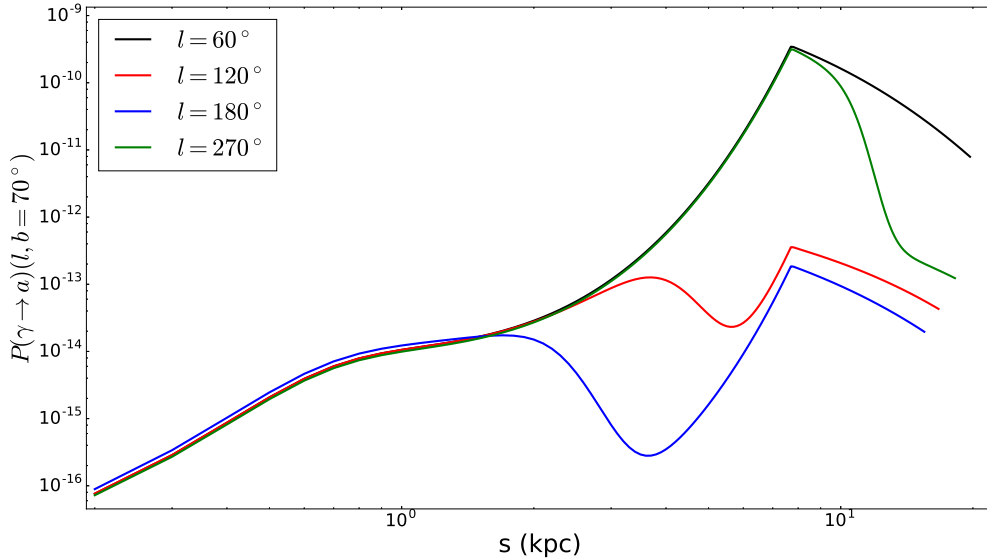


Figure 7: Probability of photon-ALP conversion at photon frequency $\nu = 500$ GHz as a function of distance s from Sun for different sky directions with the large scale Galactic magnetic field from Jansson et al. [78] and the electron density model from Cordes et al. [122] with the revised parameters according to Gaensler et al. [128]. We assumed that the outer distribution of electron goes to a constant value [121] giving the sharp change in curve at large distances.

field and electron density mentioned above, we obtain map of the maximum photon-ALPs conversion probability $P(\gamma \rightarrow a)(\hat{n})$ as a function of the direction of the sky in Fig. 6 using HEALPix [114] with $n_{\text{side}}=1024$.

From Eq. 2.26 we see that for the Galactic parameters we will have adiabatic evolution for scales $\gtrsim 10^{-4}$ pc,

$$\gamma_{\text{ad}} \approx 2 \left(\frac{n_e}{10^{-5} \text{ cm}^{-3}} \right)^2 \left(\frac{10^{-10} \text{ GeV}^{-1}}{g_{\gamma a}} \right) \left(\frac{1 \mu\text{G}}{B_T} \right) \left(\frac{10^4 \text{ pc}^{-1}}{k_B} \right) \quad (4.1)$$

a condition easily satisfied by the large scale average magnetic field and electron distribution. For adiabatic evolution (Eq. 2.16) the final conversion probability in the large scale coherent magnetic field of the Galaxy would be decided by the mixing angles very close to us in the high density region of the Galaxy. In Fig. 7 we show the evolution of the $P(\gamma \rightarrow a)$ from outskirts of the Galactic halo to solar neighborhood. The final conversion probability is given by the value near the observer which is many orders of magnitude smaller than the maximum value at around 8 kpc (see also Fig. 6). Thus for all practical purposes we CMB spectral distortion contribution from the large scale morphology of the Galactic magnetic field can be neglected if we do not take into account the turbulence in the interstellar medium.

4.2 Random magnetic field and turbulent gas

We can see from Eq. 2.15 that there are two ways to avoid adiabatic evolution: large gradients in either the magnetic field B_T or photon effective mass m_{eff} . There is observational evidence

for turbulence in the interstellar electrons from 100 pc scales down to sub-parsec scales [133] with Kolmogorov like power law. If the source of gas turbulence is magneto-hydrodynamics (MHD), we should expect stochastic magnetic fields on sub-parsec scales also. For turbulence on scales $s = 10^{-4}$ pc in regions of size $R \sim 1000$ pc we get

$$\begin{aligned} \bar{P}(\gamma \rightarrow a) &\approx \frac{P(\gamma \rightarrow a)R}{2s} \\ &\approx \frac{\Delta_{\gamma a}^2 R s}{2} = 10^{-9} \left(\frac{g_{\gamma a}}{10^{-10} \text{ GeV}^{-1}} \right)^2 \left(\frac{B_T}{1 \mu\text{G}} \right)^2 \left(\frac{R}{1000\text{pc}} \right) \left(\frac{s}{10^{-4} \text{ pc}} \right) \end{aligned} \quad (4.2)$$

These distortions as well as the cosmological distortions from random magnetic fields in voids would be unpolarized.

5 Forecasts for CORE, LiteBIRD and PIXIE

The detectability of the temperature and polarization spectral distortions in the CMB would depend on sensitivity as well as frequency coverage and number of channels of a CMB experiment. The frequency coverage (i.e. channels covering the full CMB spectrum from Rayleigh-Jeans to Wien region) and sufficient number of frequency channels are essential if we are to distinguish between the axion spectral distortions, primary CMB anisotropies, y -type and μ -type distortions and Galactic and extragalactic foregrounds. In the case of anisotropic axion distortions coming from the photon-ALP conversion in the Galactic magnetic field, we can also use the morphology of the predicted signal to distinguish it from other components.

To estimate the detectability of the signal from CMB missions using the spectrum information alone, we do a Fisher matrix analysis [134]. In reality we will also have spatial anisotropy information from the Galactic model or looking towards known voids. Our estimates from Fisher analysis should therefore be considered conservative. We model the observed intensity difference from the Planck spectrum with temperature $T_{\text{CMB}} = 2.7255$ K, ΔI_ν , as

$$\Delta I_\nu = \Delta T_{\text{CMB}} s_\nu^{\text{CMB}} + A_{\gamma a} s_\nu^{\gamma a} + y s_\nu^y + A_{\text{sync}} s_\nu^{\text{sync}} + A_{\text{Dust}} s_\nu^{\text{Dust}}, \quad (5.1)$$

here we have defined [135, 136]

$$\begin{aligned} s_\nu^{\text{sync}} &= \left(\frac{2k_B \nu^2}{c^2} \right) \left(\frac{\nu_s}{\nu} \right)^\alpha, \quad \nu_s = 30 \text{ GHz}, \\ s_\nu^{\text{CMB}} &= \frac{2k_B \nu^2}{c^2} \frac{x^2 e^x}{(e^x - 1)^2}, \quad x = h\nu / (k_B T_{\text{CMB}}), \quad T_{\text{CMB}} = 2.7255 \text{ K}, \\ s_\nu^{\text{Dust}} &= \frac{2k_B \nu^2}{c^2} \left(\frac{\nu}{\nu_0} \right)^{\beta_d + 1} \left(\frac{e^{h\nu_0 / (k_B T_d)} - 1}{e^{h\nu / (k_B T_d)} - 1} \right), \quad T_d = 18 \text{ K}, \quad \nu_0 = 545 \text{ GHz}, \\ s_\nu^y &= \frac{2h\nu^3}{c^2} \left(\frac{x e^x}{(e^x - 1)^2} \right) \left(\frac{x(e^x + 1)}{e^x - 1} - 4 \right), \end{aligned} \quad (5.2)$$

where ΔT_{CMB} is the CMB temperature anisotropy in CMB temperature units of K_{CMB} , A_{Dust} is the brightness temperature of dust at $\nu_0 = 545$ GHz and y is the dimensionless amplitude of the y -type distortion or the thermal Sunyaev-Zeldovich (tSZ) effect.

For the resonant conversion case, we can write for the 100% polarized signal,

$$s_{\nu}^{\gamma a} = \frac{h\nu^3}{c^2} \left(\frac{\nu}{\nu_0} \right) \frac{\mathcal{I}^{\gamma a}(\nu_0, m_a)}{(e^x - 1)}, \quad (5.3)$$

where $-\mathcal{I}^{\gamma a}(\nu_0, m_a)$ is the probability of conversion at $\nu_0 = 150$ GHz for axion mass m_a for the fiducial Galactic model (see Eq. 3.1) with coupling $g_{\gamma a} = 10^{-10} \text{ GeV}^{-1}$ and the dimensionless amplitude is defined as

$$A_{\gamma a} \equiv \left(\frac{g_{\gamma a}}{10^{-10} \text{ GeV}^{-1}} \right)^2 \quad (5.4)$$

This polarized distortion is not degenerate with the Sunyaev-Zeldovich effect or the y -type distortion [16] and we can ignore the y component while fitting for it. The polarization pattern of this distortion will also be very different from the CMB primary and lensing polarization. In particular polarized axion distortion will have both E and B modes. We will therefore assume that the morphological information will separate the polarized axion distortion from the CMB primary and lensing polarization signals. The only serious contamination is therefore expected from the Galactic dust emission and also synchrotron emission if the low frequency channels (below 100 GHz) are also used. We use the complete frequency range and include synchrotron as well as dust contaminations in the Fisher analysis. We also do an analysis with only dust and frequency channels higher than 100 GHz and compare the Fisher matrix forecasts in Table 2. We see that the presence of synchrotron radiation degrades constraints by a factor of ~ 2 . Future experiments like CBASS [137] and NEXTBASS² can make improvements in understanding the synchrotron emissions at low frequency. Use of these experiments jointly with LiteBIRD and CORE will improve measurability of the signal. By using the unique spatial structure of the photon-axion conversion signal, one can perform a spatial template base search in the data. This will enable further improvements in the Fisher estimates. So, our estimates presented here are very conservative and expected to improve in the future.

For the non-resonant conversion we have,

$$s_{\nu}^{\gamma a} = \left(\frac{2h\nu^3}{c^2} \right) \frac{\mathcal{I}^{\gamma a}(R, s)}{(e^x - 1)}, \quad (5.5)$$

where $-\mathcal{I}(R, s)$ is the frequency independent probability of conversion of unpolarized intensity (Eqns. 2.13, 2.27, 4.2) for turbulent magnetic fields of coherence length s for photons traversing a distance R for coupling $g_{\gamma a} = 10^{-10} \text{ GeV}^{-1}$ and the dimensionless amplitude in this case is defined as

$$A_{\gamma a} \equiv \left(\frac{g_{\gamma a} B_T^{\text{rms}}}{10^{-10} \text{ GeV}^{-1} \text{ nG}} \right)^2 \quad : \text{ voids}, \quad (5.6)$$

$$A_{\gamma a} \equiv \left(\frac{g_{\gamma a} B_T^{\text{rms}}}{10^{-10} \text{ GeV}^{-1} \mu\text{G}} \right)^2 \quad : \text{ Galaxy}, \quad (5.7)$$

where B_T^{rms} is the magnetic field strength on scales s . In this case the distortion is unpolarized and we must marginalize over the y -type distortion and CMB anisotropies.

²<https://www2.physics.ox.ac.uk/research/experimental-radio-cosmology/the-next-band-all-sky-survey-nextbass>

The spectrum of each of the signal is plotted in Fig. 8 with the amplitudes chosen so that the intensities are of similar amplitude allowing us to compare the shapes of the spectra. The detectability of photon-ALP conversion depends upon the error budget of a particular mission, its frequency coverage and number of frequency channels available. The measurability of a non-degenerate parameter (p_i) depends upon the covariance matrix (\mathcal{C}_{ii}), which in turn depends upon the inverse of the Fisher matrix elements ($\mathcal{C}_{ii} = 1/F_{ii}$) [134]. The elements of Fisher matrix for a set of parameters $\mathcal{P} = (p_1, p_2, \dots, p_n)$ are defined as [134]

$$F_{ij} = \sum_{\alpha=1}^n \frac{\partial \Delta s(\nu_\alpha)}{\partial p_i} \frac{1}{(\Delta s_\nu^n)^2} \frac{\partial \Delta s(\nu_\alpha)}{\partial p_j}, \quad (5.8)$$

where, the sum is made over all frequency channels and Δs_ν^n denotes the value of instrumental noise specific to a particular mission. For the degenerate parameters the Fisher matrix is not diagonal. The elements of covariance matrix in this case are computed from the inverse of the Fisher Matrix ($\mathcal{C}_{ij} = (F^{-1})_{ij}$). We use the model given in Eq. (5.1), with the parameter vector for resonant polarized distortion given by $\mathcal{P} = (A_{\gamma_a}, A_{\text{Dust}}, \beta_d, \alpha, A_{\text{sync}})$ and for non-resonant unpolarized distortion given by $\mathcal{P} = (\Delta T_{\text{CMB}}, A_{\gamma_a}, A_{\text{Dust}}, \beta_d, y, \alpha, A_{\text{sync}})$. We calculate the Fisher matrix at following fiducial values of foreground model, $A_d = 100 \mu\text{K}$ at 545 GHz, $\beta_d = 1.5$, $A_{\text{sync}} = 150 \mu\text{K}$ at 30 GHz, $\alpha = 2.8$ [135].

5.1 Future constraints from the unpolarized axion distortion (non-resonant conversion)

The results of the Fisher analysis are shown in Fig. 9 for future CMB missions like PIXIE [42], CORE [48] and LiteBIRD [49] and also for a mission with 10 times better sensitivity than PIXIE. The Fisher analysis are performed for two scenarios, (i) with only dust as the foreground contaminations and (ii) with both synchrotron and dust contaminations. For case (i), we have used the frequency channels between 100 – 600 GHz for PIXIE and CORE and 100 – 402 GHz for LiteBIRD with the corresponding instrumental noise mentioned in Table 1, $f_{\text{sky}} = 1$ and using Eq. 5.1 for the estimation. We have marginalized out CMB & dust and obtained the contour for y distortion and A_{γ_a} for photon-axion conversion in the turbulent magnetic field in voids and in our Galaxy. For the case (ii), we used all the frequency channels provided in Table 1 and have marginalized over the amplitude as well as the spectral index of synchrotron and dust in the Fisher analysis. The CORE Fisher estimates gets worse by nearly a factor of ~ 5 , after considering both synchrotron and dust due to the absence of a few low frequency channels. For missions like LiteBird and PIXIE, the constraints degrades constraints by a factor of ~ 2 . The Fisher estimates presented here are conservative and can be further improved by using the spatial template of the photon-axion conversion signal.

The signal and thus our constraints depend not only on the quantity the coupling g_{γ_a} and magnetic field strength B_T^{rms} which make up the amplitude A_{γ_a} (Eq. 5.6, 5.7) but also the void or Galaxy model as shown in Eqs. (2.27) and (4.2) respectively. We can rescale the constraints for different void or Galactic model using Eqns. 2.27 and 4.2. The constraints in Fig. 9 for the voids are for the parameters mentioned in Eq. (2.27) with $R_v = 1$ Gpc and $s_v = 10$ pc. For the Galaxy, the forecasts are obtained for $R_g = 1$ kpc and $s_g = 10^{-4}$ pc. Our results show that the turbulent component of the voids can impose stronger constraints than the Galaxy. This is because of larger scale (R) of the voids as well as the larger turbulence

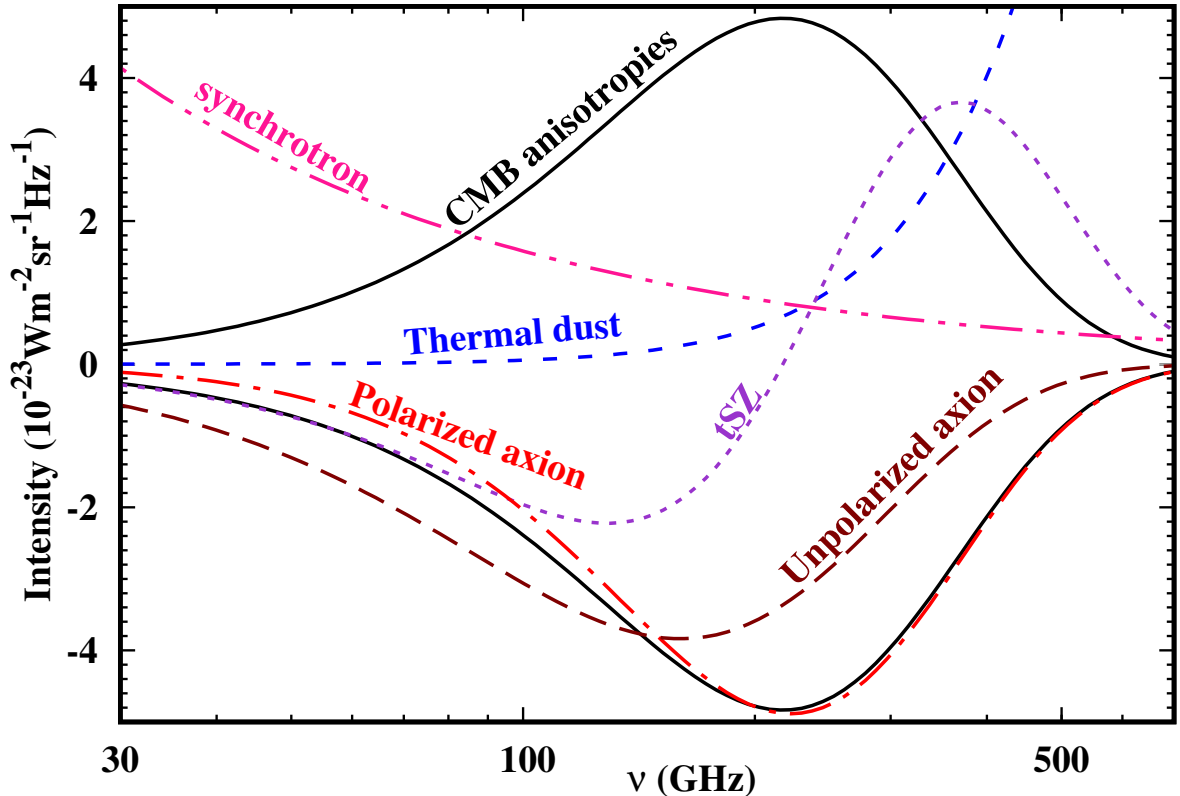


Figure 8: The spectra of the components mentioned in Eq. (5.1) are compared with $A_{\text{CMB}} = \pm 10 \mu\text{K}$ for the CMB anisotropies, $A_{\text{dust}} = 1 \mu\text{K}$ at 545 GHz for thermal dust emission, $A_y = 2 \times 10^{-6}$ for thermal Sunyaev-Zeldovich (tSZ) effect, $\beta_d = 1.4$ [135], for synchrotron $A_{\text{sync}} = 150 \mu\text{K}$ at 30 GHz, $\alpha = 2.8$ [136], $A_{\gamma_a} = 20$, $\bar{\mathcal{I}}(m_a = 5 \times 10^{-13} \text{ eV}) = -10^{-6}$ for polarized axion distortion and $A_{\gamma_a} \bar{\mathcal{I}} = -10^{-5}$ for the unpolarized axion distortion.

scale (s) when the propagation becomes non-adiabatic compared to the Galaxy. The larger non-adiabaticity scale (s) is in turn the result of small electron densities in the voids (Eq. 2.26). We should therefore expect strongest constraints from the emptiest voids for the same magnetic field strength. Stacking the known voids from other cosmological probes could also improve the SNR and we leave a detailed study with more realistic void profile and magnetic field spectrum for future work.

5.2 Future constraints from the polarized anisotropic axion distortion (resonant conversion)

The 100% polarized anisotropic spectral distortion from the resonant conversion in the Galactic magnetic field can evade the contamination from statistically isotropic y -distortion and CMB anisotropies due to its characteristic polarization pattern in the sky. We can therefore assume that these components would be separated using the morphological and polarization information and ignore them for the Fisher analysis. The only significant contamination we must distinguish (above 100 GHz) is then the Galactic dust contamination. In Fig. 10, we plot the possible constraints which can be obtained from the polarized signal in presence of synchrotron and dust after marginalizing over α , A_{sync} , β_d . We use the mean signal calculated in Sec. 3 and Fig. 5 from the parts of the sky with signal $\Delta I_\nu / I_\nu > 10^{-10}$. This selects

Table 1: Instrumental noise for different missions

Mission	Frequency Channels (GHz)	Instrumental noise	All sky sensitivity ($10^{-27}\text{Wm}^{-2}\text{sr}^{-1}\text{Hz}^{-1}$)	Duration (Months)
PIXIE	30-600 $\Delta\nu = 15$	($\Delta I_\nu^I = 4 \times 10^{-24}$ & $\Delta I_\nu^P = 6 \times 10^{-25}$) $\text{Wm}^{-2}\text{Hz}^{-1}\text{sr}^{-1}$ per pixel. Total number of Pixels (N)= 49152	$\Delta I_\nu^I = 18$ $\Delta I_\nu^P = 2.7$	48
LiteBIRD	40, 50, 60, 68, 78, 89, 100, 119, 140, 166, 195, 235, 280, 338, 402	$w_T^{-1/2} = (26, 16.7, 13.8, 11.2, 9.4, 8.1, 6.4, 5.3, 4.1, 4.5, 4.0, 5.3, 9.2, 13.5, 26.1) \mu\text{K}$ arcmin $w_P^{-1/2} = (36.8, 23.6, 19.5, 15.9, 13.3, 11.5, 9.0, 7.5, 5.8, 6.3, 5.7, 7.5, 13.0, 19.1, 36.9) \mu\text{K}$ arcmin	$\Delta I_\nu^I = (1, 0.98, 1.14, 1.15, 1.23, 1.32, 1.25, 1.3, 1.25, 1.6, 1.55, 2.1, 3.2, 3.6, 4.5)$ $\Delta I_\nu^P = (1.42, 1.4, 1.6, 1.64, 1.74, 1.88, 1.8, 1.9, 1.8, 2.2, 2.2, 2.9, 4.8, 5.1, 6.3)$	36
CORE	60, 70, 80, 90, 100, 115, 130, 145, 160, 175, 195, 220, 255, 295, 340, 390, 450, 520, 600	$w_T^{-1/2} = (7.5, 7.1, 6.8, 5.1, 5.0, 5.0, 3.9, 3.6, 3.7, 3.6, 3.5, 3.8, 5.6, 7.4, 11.1, 22.0, 45.9, 116.6, 358.3) \mu\text{K}$ arcmin $w_P^{-1/2} = (10.6, 10.0, 9.6, 7.3, 7.1, 7.0, 5.5, 5.1, 5.2, 5.1, 4.9, 5.4, 7.9, 10.5, 15.7, 31.1, 64.9, 164.8, 506.7) \mu\text{K}$ arcmin	$\Delta I_\nu^I = (0.62, 0.77, 0.93, 0.84, 1.0, 1.2, 1.1, 1.1, 1.3, 1.3, 1.4, 1.5, 2.1, 2.5, 2.9, 4.1, 5.3, 7.0, 9.3)$ $\Delta I_\nu^P = (0.88, 1.09, 1.31, 1.21, 1.4, 1.7, 1.5, 1.6, 1.8, 1.9, 1.9, 2.1, 3.0, 3.5, 4.1, 5.9, 7.5, 9.9, 13)$	36

a fraction of sky $f_{sky} = 0.68$ for axion mass $m_a = 5 \times 10^{-12}$ eV with average distortion $\bar{\mathcal{I}}(\nu = 150 \text{ GHz}) = 8.3 \times 10^{-8}$ and $f_{sky} = 0.4$ for axion mass $m_a = 5 \times 10^{-13}$ eV with average distortion in this fraction of sky of $\bar{\mathcal{I}}(\nu = 150 \text{ GHz}) = 1.1 \times 10^{-6}$ for $g_{\gamma a} = 10^{-10} \text{ GeV}^{-1}$. We do the Fisher analysis for the two axion masses using these mean distortions. The signal for low mass axions is stronger and hence can be better constrained at high latitudes in comparison to the signal from high mass axions (see Eq. 3.1 and Sec. 3) because the resonance happens further out in the Galaxy where the electron density is smaller. Our knowledge of electron distribution and magnetic fields in the Galaxy should improve considerably in not far future, on the similar timescales as the future CMB missions. We should therefore expect strong direct constraints on the photon-axion coupling from the polarized anisotropic distortions of the CMB in the future in the axion mass range where resonances can occur in

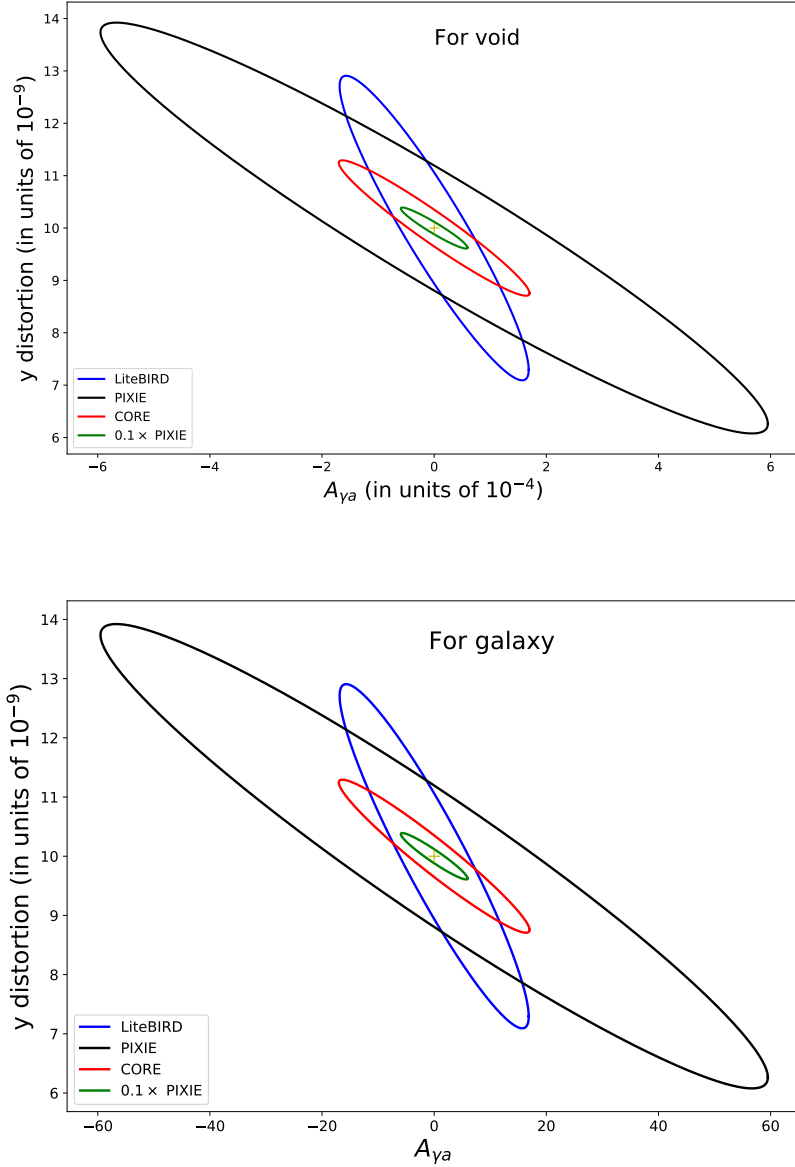


Figure 9: 68% contour between y distortion and $A_{\gamma_a} \propto (g_{\gamma_a} B_T^{\text{rms}})^2$ (defined in Eq. 5.7 for the Galaxy and Eq. 5.6 for the voids) for different future missions. In green (the smallest contour), we plot for a case with instrumental noise better than PIXIE by a factor of 10.

the Galactic halo. A Fisher forecast for different combinations of the foreground is presented in Table 2. The second column of Table 2 is obtained with only dust as the foreground contaminations and we used frequency channels above 100 GHz. The Fisher forecasts for the more realistic situation including both synchrotron and dust and using all frequency channels are shown in the second column in Table 2. The presence of synchrotron degrades the constraints by little more than a factor of 2.

Table 2: Fisher forecast for two different combinations of foregrounds Dust (D) and Synchrotron (S). For dust (D) only case, we used channels only above 100 GHz. For dust and synchrotron (S+D) case, we used all the frequency channels shown in Table 1. The constraints we get for S+D case are around 2 times weaker compared to the case when only dust foreground is present. For CORE, the constraints degrades by around 5 times due to the absence of low frequency channels. These estimates are conservative and can be improved by using the unique spatial structure of the photon-axion conservation signal.

Probe	$[F^{-1}]_{ii}$ with D only			$[F^{-1}]_{ii}$ with S+D		
	PIXIE	LiteBIRD	CORE	PIXIE	LiteBIRD	CORE
g_{10}^2 for $m_a = 5 \times 10^{-13}$ eV ($\times 10^{-3}$)	0.62	1.92	0.83	1.29	3.5	2.28
$A_{\gamma a}$ for void ($\times 10^{-4}$)	1.63	0.48	0.23	3.9	1.1	1.12
$A_{\gamma a}$ for galaxy	16.3	4.83	2.25	39	11.1	11.2

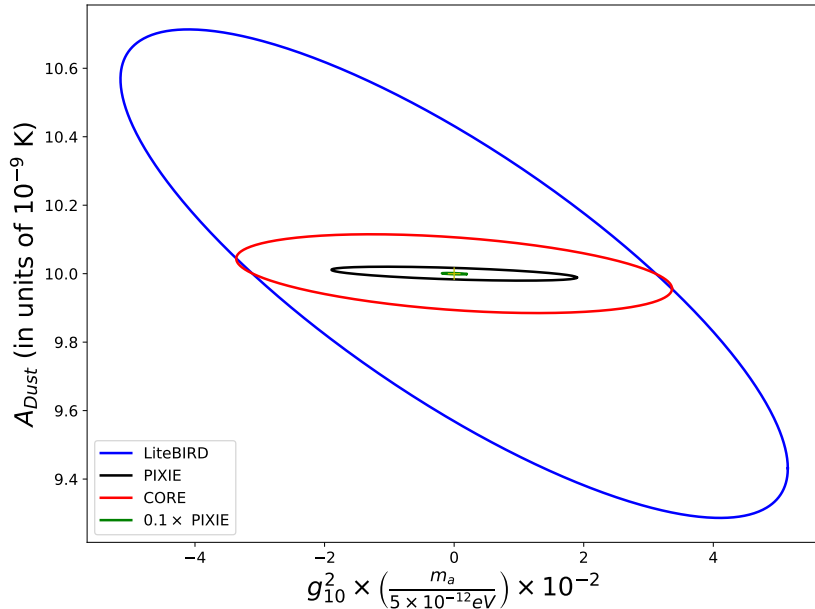


Figure 10: 68% contour between dust contamination A_{Dust} and $g_{\gamma a}^2 \times \left(\frac{m_a}{5 \times 10^{-12}}\right)$ for the proposed specifications of different future missions from the polarized anisotropic spectral distortions of the CMB. In green, (the smallest contour) we plot the case with 10 times better sensitivity than PIXIE. The magnitude of $g_{\gamma a}$ is expressed in units of $g_{10} = 10^{-10}$ GeV $^{-1}$ with the average signal $\bar{\mathcal{I}} = 8.3 \times 10^{-8}$ and 1.1×10^{-6} for $m_a = 5 \times 10^{-12}$ eV and 5×10^{-13} eV respectively.

5.3 Comparison with other experiments

We compare CMB forecasts with with the current bounds from CAST experiment [69], SN1987A [138] and X-ray bounds from Coma cluster [139] in Fig. 11. The 95% upper limits are shown. The future CMB missions can therefore provide competitive constraints com-

pared with the lab experiments such as CAST. Other bounds [57] available in the literature have looked at the extragalactic scenario with a much lower value of n_e and magnetic field. The bounds on $g_{\gamma a} B_T$ by Tashiro et al. [58] are obtained using the primordial magnetic field with value today of the order nG. Other astrophysical constraints are from the measurement of gamma ray signal from SN 1987A ($g_{\gamma a} \leq 5.3 \times 10^{-12} \text{ GeV}^{-1}$) [138] and from X-ray observations of the Coma cluster ($g_{\gamma a} \leq 1.4 \times 10^{-12} \text{ GeV}^{-1}$) [139].

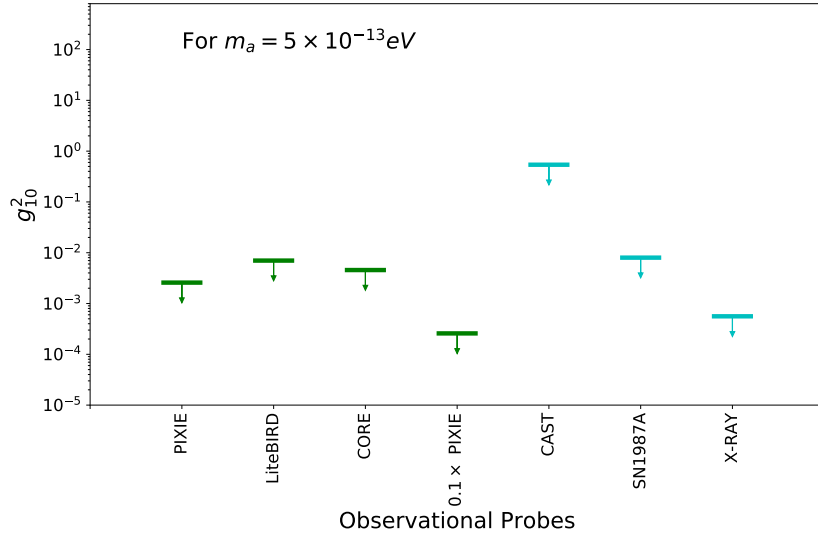
6 Conclusions

We have studied a new avenue of spectral distortion of CMB photons due to photon-ALP and photon-LSP conversion in presence of our local magnetic field of Milky way. We consider both resonant (Sec. 3) and non-resonant (Sec. 4) Photon-ALP and photon-LSP conversions. Even though we have done our calculations specifically for pseudoscalars such as axions, our results apply, with trivial correspondence between the coupling constants and rotation of the polarization by 90° , almost unchanged to the scalar particles. The only observable difference between the scalar and pseudoscalars is that in the case where we have a polarized signal, the polarization of the distortion (photons which disappear due to conversion to scalars or pseudoscalars) is along the direction of the transverse magnetic field in case of pseudoscalars (Eq. 2.1) and in the orthogonal direction in the case of scalar particles. (Eq. 3.4).

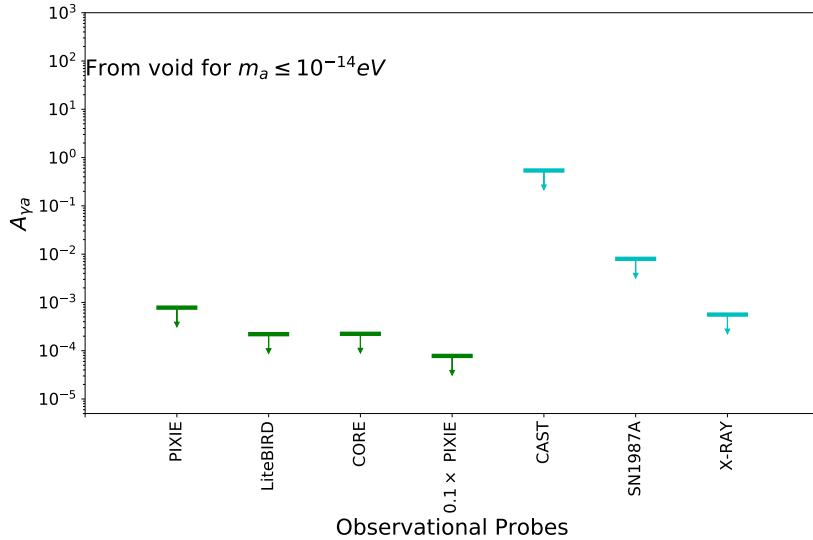
The resonant conversions can happen in the Galactic halo for $10^{-14} \text{ eV} \lesssim m_a \lesssim 10^{-11} \text{ eV}$. The probability of conversion depends on the electron distribution as well as the large scale magnetic field structure of the Galaxy imparting a characteristic anisotropy to the spectral distortion. In addition this distortion is 100% polarized. The polarized anisotropic spectral distortion provides an ideal target for future CMB missions which would focus on the polarized signals. The anisotropic nature of the signal means that it is accessible by the CMB experiments without absolute calibration. The polarization of the signal for scalars and pseudoscalars is orthogonal to each other. In this very interesting case, we therefore get the mass of the particle from the anisotropy pattern, which varies with the particle mass, and from the polarization we can tell whether the particle coupled to photons is a scalar or a pseudoscalar particle.

For axion masses $m_a \lesssim 10^{-14} \text{ eV}$ we consider non-resonant conversion in the small scale turbulent Galactic magnetic field as well as the primordial stochastic magnetic fields in the voids. This distortion is unpolarized if it is the average over large number of random magnetic field configurations. If the small scale turbulent magnetic fields in the Galaxy are correlated with the large scale magnetic field structure [77], then we would expect an anisotropy similar to that shown in Fig. 6. The CMB spectral distortions from non-resonant conversion depends sensitively on the model of turbulent magnetic fields in the Galaxy and in the voids as well as the electron density profiles. We have used a simplified model for Fisher matrix analysis to estimate the level of distortion and the constraints on photon-axion coupling accessible by these distortions. Our results are encouraging and motivate a more detailed analysis with realistic models of voids and Galaxy in the future.

We have also shown that the strong cosmological constraints for $10^{-14} \lesssim m_a \lesssim 5 \times 10^{-13} \text{ eV}$ claimed by [58] are invalid. For lower ALP masses constraints were obtained on non-resonant photon-axion conversion in stochastic magnetic fields using a toy model with magnetic field abruptly changing direction on Mpc scales in [57]. We have shown that the constraints from a more realistic primordial magnetic field model are much weaker thus



(a) From polarized resonance conversion



(b) From unpolarized non-resonance conversion

Figure 11: Assuming a Gaussian probability distribution function, 2σ upper limit achievable on (a) g_{10}^2 for resonant conversion in the Galactic magnetic field for $m_a = 5 \times 10^{-13}$ eV and (b) on $A_{\gamma a} \propto (g_{\gamma a} B_T^{\text{rms}})^2$ for non-resonant conversion in voids are shown for different CMB missions with conservative marginalization over both dust and synchrotron. We also plot the 95% upper bound only on g_{10}^2 (cyan) from ground based experiment CAST [69], the gamma ray flux of SN1987A [138] and from X-ray observations of the Coma cluster [139].

illustrating the sensitivity of the photon-axion conversion on the assumptions about the intergalactic magnetic fields.

We have used the mean signal for the Fisher matrix analysis in the case of resonant conversion in the Galactic halo. However as we can see from the maps in Fig. 5, there is large anisotropy in the signal with the signal varying by many orders of magnitude over the sky. In particular there are regions in the sky with much higher signal than the mean. We have also not used all channels available in the CMB experiments (like PIXIE) to simplify the analysis. Using higher frequency channels would require a more sophisticated model of dust emission than our 2-parameter model. Using additional channels would help improve the sensitivity and thus our constraints. Our results however rely on the knowledge of Galactic electron distribution and magnetic fields which we expect to improve significantly with the future radio surveys, in particular with the Square Kilometer Array [132] on time scales similar to the proposed CMB space missions.

Acknowledgements This work has been done within the Labex ILP (reference ANR-10-LABX-63) part of the IDEX SUPER, and received financial state aid managed by the Agence Nationale de la Recherche, as part of the programme Investissements d’avenir under the reference ANR-11-IDEX-0004-02. The work of SM and BDW are supported by the Simons Foundation. This research was supported by SERB grant no. ECR/2015/000078 of Science and Engineering Research board, Dept. of Science and Technology, Govt. of India. This research was also supported by Max-Planck-Gesellschaft through the partner group between MPI for Astrophysics, Garching and TIFR, Mumbai. This research made use of computational resources of IAP, CCA and DTP-TIFR. RK would like to thank Max Planck Institute for Astrophysics, Garching for hospitality where part of this work was done. RK would like to thank Basudeb Dasgupta and Amol Dighe for numerous discussions and help in understanding the flavor oscillation physics and to the former for also reading the manuscript and making useful comments. SM would like to thank Joseph Silk for useful discussions and comments on the draft. The authors also acknowledge valuable comments from David Spergel, David Marsh, Eiichiro Komatsu and Hendrik Vogel on the paper.

A Galactic magnetic field and electron density model

A model of the coherent component of the Galactic magnetic field in the disk and halo of Milky way was developed by Jansson et al. [78]. Magnetic field in the Galactic halo at a radius r and height l can be written into toroidal (B^{tor}) and poloidal (B^{pol}) component in terms of step function $L(l, h, w) = (1 + e^{-2(|l-h|/w)})^{-1}$. The toroidal component is separated into the north (B_n) and south (B_s) component as [78]

$$B^{\text{tor}}(r, l) = e^{-|l|/l_0} L(l, h_{\text{disk}}, w_{\text{disk}}) \times \begin{cases} B_n (1 - L(r, r_n, w_h)) & l > 0, \\ B_s (1 - L(r, r_s, w_h)) & l < 0, \end{cases} \quad (\text{A.1})$$

The step function $L(l, h, w)$ goes to zero for $l \rightarrow 0, h \gg w$ and unity at $l \gg h$. The first factor of L means that we restrict the toroidal component to outside the disk of height h_{disk} and the second factor of L makes the field diminish outside a radius of r_n, r_s for the northern

and southern regions of the Galaxy respectively.

$$B^{\text{pol}}(r, l) = B_X e^{-r_p/r_X} \times \begin{cases} \left(\frac{r_p}{r}\right), & \text{with } r_p = r - |l|/\tan(\Theta_X^0)r > r_X, \\ \left(\frac{r_p}{r}\right)^2, & \text{with } r_p = \frac{rr_X^c}{r_X^c + |l|/\tan(\Theta_X^0)} r < r_X \text{ \&} \\ \Theta_X(r, l) = \tan^{-1}\left(\frac{|l|}{r-r_p}\right). \end{cases} \quad (\text{A.2})$$

The following best fit parameters for the toroidal and poloidal components of the magnetic field are fitted by [78]: $l_0 = 5.3 \pm 1.6$ kpc, $r_n = 9.22 \pm 0.08$ kpc, $r_s > 16.7$ kpc, $w_h = 0.2 \pm 0.02$ kpc, $h_{\text{disk}} = 0.4 \pm 0.03$ kpc, $w_{\text{disk}} = 0.27 \pm 0.08$ kpc, $B_n = 1.4 \pm 0.1 \mu\text{G}$, $B_s = -1.1 \pm 0.1 \mu\text{G}$, $B_X = 4.6 \mu\text{G}$, $\Theta_X^0 = 49 \pm 1^\circ$, $r_X^c = 4.8 \pm 0.2$ kpc, $r_X = 2.9 \pm 0.1$ kpc.

The electron density decreases exponentially with increasing distance from the Galactic plane [121, 122, 128]. The electron density in the Galactic halo can be modeled as $\text{sech}^2(|l|/H)$ [122].

$$n_e(r, l) = n_1 \left[\frac{\cos(\pi r/2A_1)}{\cos(\pi R_\odot/2A_1)} \right] \text{sech}^2(|l|/H) U(r - A_1), \quad (\text{A.3})$$

where, $U(x)$ is a step function. The value of vertical scale height of $H = 0.95$ kpc was used by Cordes et al. [122], which was later modified to $H = 1.8$ kpc by Gaensler et al. [128] and $A_1 = 17$ kpc, $n_1 = 0.035 \text{cm}^{-3}$. This indicates a much higher electron density at high latitudes than the previous analysis [122]. Similar to the paper by Jansson et al. [78] (which provides the model for the magnetic field), we use the model of electron density given by Cordes et al. [122] with the improved model parameters from Gaensler et al. [128].

The estimation of photon-ALP conversion depends on the model of the magnetic field and electron density in the high latitudes. In particular, for the toroidal component, the magnetic field strength drops exponentially with a scale height of $l = 5.3$ kpc. The electron density also decreases exponentially with increasing distance from the Galactic plane [121, 122, 128]. Current observations do not provide a good probe for the electron density in the Galactic halo. However, from the upcoming mission SKA [132] an accurate observation of electron density can improve the constraints on the value of n_e and B . In this paper, we will assume the electron density model of Cordes et al. [122] with the parameter values according to Gaensler et al. [128].

References

- [1] A. A. Penzias and R. W. Wilson. A Measurement of Excess Antenna Temperature at 4080 Mc/s. *ApJ*, 142:419–421, July 1965. [DOI], [ADS].
- [2] D. J. Fixsen, E. S. Cheng, J. M. Gales, J. C. Mather, R. A. Shafer, and E. L. Wright. The Cosmic Microwave Background Spectrum from the Full COBE FIRAS Data Set. *ApJ*, 473:576, 1996. [DOI], [ADS].
- [3] D. J. Fixsen, G. Hinshaw, C. L. Bennett, and J. C. Mather. The Spectrum of the Cosmic Microwave Background Anisotropy from the Combined COBE FIRAS and DMR Observations. *ApJ*, 486:623–628, September 1997. arXiv:astro-ph/9704176, [DOI], [ADS].
- [4] D. J. Fixsen and J. C. Mather. The Spectral Results of the Far-Infrared Absolute Spectrophotometer Instrument on COBE. *ApJ*, 581:817–822, 2002. [DOI], [ADS].

- [5] D. J. Fixsen. The Temperature of the Cosmic Microwave Background. *ApJ*, 707:916–920, December 2009. [arXiv:0911.1955](#), [\[DOI\]](#), [\[ADS\]](#).
- [6] H. P. Gush, M. Halpern, and E. H. Wishnow. Rocket measurement of the cosmic-background-radiation mm-wave spectrum. *Physical Review Letters*, 65:537–540, July 1990. [\[DOI\]](#), [\[ADS\]](#).
- [7] E. L. Wright, C. L. Bennett, K. Gorski, G. Hinshaw, and G. F. Smoot. Angular Power Spectrum of the Cosmic Microwave Background Anisotropy seen by the COBE DMR. *ApJL*, 464:L21, 1996. [\[DOI\]](#), [\[ADS\]](#).
- [8] C. L. Bennett, D. Larson, J. L. Weiland, N. Jarosik, G. Hinshaw, N. Odegard, K. M. Smith, R. S. Hill, B. Gold, M. Halpern, E. Komatsu, M. R. Nolta, L. Page, D. N. Spergel, E. Wollack, J. Dunkley, A. Kogut, M. Limon, S. S. Meyer, G. S. Tucker, and E. L. Wright. Nine-year Wilkinson Microwave Anisotropy Probe (WMAP) Observations: Final Maps and Results. *ApJS*, 208:20, October 2013. [arXiv:1212.5225](#), [\[DOI\]](#), [\[ADS\]](#).
- [9] Planck Collaboration, R. Adam, P. A. R. Ade, N. Aghanim, Y. Akrami, M. I. R. Alves, F. Argüeso, M. Arnaud, F. Arroja, M. Ashdown, and et al. Planck 2015 results. I. Overview of products and scientific results. *A&A*, 594:A1, September 2016. [arXiv:1502.01582](#), [\[DOI\]](#), [\[ADS\]](#).
- [10] D. Hanson et al. Detection of B-Mode Polarization in the Cosmic Microwave Background with Data from the South Pole Telescope. *Physical Review Letters*, 111(14):141301, October 2013. [arXiv:1307.5830](#), [\[DOI\]](#), [\[ADS\]](#).
- [11] S. Das et al. Detection of the Power Spectrum of Cosmic Microwave Background Lensing by the Atacama Cosmology Telescope. *Physical Review Letters*, 107(2):021301, July 2011. [arXiv:1103.2124](#), [\[DOI\]](#), [\[ADS\]](#).
- [12] BICEP2 Collaboration and Keck Array Collaboration. BICEP2/Keck Array VIII: Measurement of Gravitational Lensing from Large-scale B-mode Polarization. *ApJ*, 833:228, December 2016. [arXiv:1606.01968](#), [\[DOI\]](#), [\[ADS\]](#).
- [13] P. A. R. Ade et al. Measurement of the Cosmic Microwave Background Polarization Lensing Power Spectrum with the POLARBEAR Experiment. *Physical Review Letters*, 113(2):021301, July 2014. [arXiv:1312.6646](#), [\[DOI\]](#), [\[ADS\]](#).
- [14] C. MacTavish et al. Cosmological Parameters from the 2003 Flight of BOOMERANG. *ApJ*, 647:799–812, August 2006. [arXiv:astro-ph/0507503](#), [\[DOI\]](#), [\[ADS\]](#).
- [15] R. Stompor, S. Hanany, M. E. Abroe, J. Borrill, P. G. Ferreira, A. H. Jaffe, B. Johnson, A. T. Lee, B. Rabii, P. L. Richards, G. Smoot, C. Winant, and J. H. P. Wu. The MAXIMA Experiment: Latest Results and Consistency Tests. *ArXiv Astrophysics e-prints*, September 2003. [arXiv:astro-ph/0309409](#), [\[ADS\]](#).
- [16] Y. B. Zeldovich and R. A. Sunyaev. The Interaction of Matter and Radiation in a Hot-Model Universe. *ApSS*, 4:301–316, 1969. [\[DOI\]](#), [\[ADS\]](#).
- [17] R. A. Sunyaev and Y. B. Zeldovich. The interaction of matter and radiation in the hot model of the Universe, II. *ApSS*, 7:20–30, 1970. [\[DOI\]](#), [\[ADS\]](#).
- [18] J. Chluba and R. A. Sunyaev. The evolution of CMB spectral distortions in the early Universe. *MNRAS*, 419:1294–1314, 2012. [\[DOI\]](#), [\[ADS\]](#).
- [19] J. Chluba, R. Khatri, and R. A. Sunyaev. CMB at 2×2 order: the dissipation of primordial acoustic waves and the observable part of the associated energy release. *MNRAS*, 425:1129–1169, September 2012. [arXiv:1202.0057](#), [\[DOI\]](#), [\[ADS\]](#).
- [20] R. Khatri and R. A. Sunyaev. Creation of the CMB spectrum: precise analytic solutions for the blackbody photosphere. *JCAP*, 6:038, June 2012. [arXiv:1203.2601](#), [\[DOI\]](#), [\[ADS\]](#).

- [21] R. Khatri, R. A. Sunyaev, and J. Chluba. Mixing of blackbodies: entropy production and dissipation of sound waves in the early Universe. *A&A*, 543:A136, July 2012. [arXiv:1205.2871](#), [\[DOI\]](#), [\[ADS\]](#).
- [22] R. Khatri and R. A. Sunyaev. Beyond y and μ : the shape of the CMB spectral distortions in the intermediate epoch, $1.5 \times 10^4 \lesssim z \lesssim 2 \times 10^5$. *JCAP*, 9:016, September 2012. [arXiv:1207.6654](#), [\[DOI\]](#), [\[ADS\]](#).
- [23] R. A. Sunyaev and R. Khatri. Unavoidable CMB Spectral Features and Blackbody Photosphere of Our Universe. *International Journal of Modern Physics D*, 22:1330014, June 2013. [arXiv:1302.6553](#), [\[DOI\]](#), [\[ADS\]](#).
- [24] J. Chluba. Which spectral distortions does Λ CDM actually predict? *MNRAS*, 460:227–239, July 2016. [arXiv:1603.02496](#), [\[DOI\]](#), [\[ADS\]](#).
- [25] J. C. Hill, N. Battaglia, J. Chluba, S. Ferraro, E. Schaan, and D. N. Spergel. Taking the Universe’s Temperature with Spectral Distortions of the Cosmic Microwave Background. *Physical Review Letters*, 115(26):261301, December 2015. [arXiv:1507.01583](#), [\[DOI\]](#), [\[ADS\]](#).
- [26] R. Emami, E. Dimastrogiovanni, J. Chluba, and M. Kamionkowski. Probing the scale dependence of non-Gaussianity with spectral distortions of the cosmic microwave background. *Phys.Rev.D*, 91(12):123531, June 2015. [arXiv:1504.00675](#), [\[DOI\]](#), [\[ADS\]](#).
- [27] Matthew Hasselfield et al. The Atacama Cosmology Telescope: Sunyaev-Zel’dovich selected galaxy clusters at 148 GHz from three seasons of data. *JCAP*, 1307:008, 2013. [arXiv:1301.0816](#), [\[DOI\]](#).
- [28] L. E. Bleem et al. Galaxy Clusters Discovered via the Sunyaev-Zel’dovich Effect in the 2500-square-degree SPT-SZ survey. *Astrophys. J. Suppl.*, 216(2):27, 2015. [arXiv:1409.0850](#), [\[DOI\]](#).
- [29] P. A. R. Ade et al. Planck 2015 results. XXVII. The Second Planck Catalogue of Sunyaev-Zeldovich Sources. *Astron. Astrophys.*, 594:A27, 2016. [arXiv:1502.01598](#), [\[DOI\]](#).
- [30] Z. Staniszewski et al. Galaxy clusters discovered with a Sunyaev-Zel’dovich effect survey. *Astrophys. J.*, 701:32–41, 2009. [arXiv:0810.1578](#), [\[DOI\]](#).
- [31] M. Zemcov et al. First detection of the Sunyaev Zel’dovich effect increment at $\lambda < 650 \mu\text{m}$. *A&A*, 518:L16, July 2010. [arXiv:1005.3824](#), [\[DOI\]](#), [\[ADS\]](#).
- [32] Planck Collaboration, P. A. R. Ade, N. Aghanim, M. Arnaud, M. Ashdown, F. Atrio-Barandela, J. Aumont, C. Baccigalupi, A. Balbi, A. J. Banday, and et al. Planck intermediate results. VIII. Filaments between interacting clusters. *A&A*, 550:A134, February 2013. [arXiv:1208.5911](#), [\[DOI\]](#), [\[ADS\]](#).
- [33] Hiroyuki Tashiro, Eray Sabancilar, and Tanmay Vachaspati. CMB Distortions from Superconducting Cosmic Strings. *Phys. Rev.*, D85:103522, 2012. [arXiv:1202.2474](#), [\[DOI\]](#).
- [34] Hiroyuki Tashiro, Eray Sabancilar, and Tanmay Vachaspati. CMB Distortions from Damping of Acoustic Waves Produced by Cosmic Strings. *JCAP*, 1308:035, 2013. [arXiv:1212.3283](#), [\[DOI\]](#).
- [35] J. Chluba. Could the cosmological recombination spectrum help us understand annihilating dark matter? *MNRAS*, 402:1195–1207, February 2010. [arXiv:0910.3663](#), [\[DOI\]](#), [\[ADS\]](#).
- [36] Sergio Colafrancesco. SZ effect from dark matter annihilation. *Astron. Astrophys.*, 422:L23–L28, 2004. [arXiv:astro-ph/0405456](#), [\[DOI\]](#).
- [37] Hiroyuki Tashiro and Naoshi Sugiyama. Constraints on Primordial Black Holes by Distortions of Cosmic Microwave Background. *Phys. Rev.*, D78:023004, 2008. [arXiv:0801.3172](#), [\[DOI\]](#).
- [38] Paolo Pani and Abraham Loeb. Constraining Primordial Black-Hole Bombs through Spectral

Distortions of the Cosmic Microwave Background. *Phys. Rev.*, D88:041301, 2013. [arXiv:1307.5176](#), [\[DOI\]](#).

- [39] Daniel Aloni, Kfir Blum, and Raphael Flauger. Cosmic microwave background constraints on primordial black hole dark matter. *JCAP*, 1705(05):017, 2017. [arXiv:1612.06811](#), [\[DOI\]](#).
- [40] R. Khatri and R. Sunyaev. Limits on the fluctuating part of y -type distortion monopole from Planck and SPT results. *JCAP*, 8:013, August 2015. [arXiv:1505.00781](#), [\[DOI\]](#), [\[ADS\]](#).
- [41] R. Khatri and R. Sunyaev. Constraints on μ -distortion fluctuations and primordial non-Gaussianity from Planck data. *JCAP*, 9:026, September 2015. [arXiv:1507.05615](#), [\[DOI\]](#), [\[ADS\]](#).
- [42] A. Kogut, D. J. Fixsen, D. T. Chuss, J. Dotson, E. Dwek, M. Halpern, G. F. Hinshaw, S. M. Meyer, S. H. Moseley, M. D. Seiffert, D. N. Spergel, and E. J. Wollack. The Primordial Inflation Explorer (PIXIE): a nulling polarimeter for cosmic microwave background observations. *JCAP*, 7:25, 2011. [arXiv:1105.2044](#), [\[DOI\]](#), [\[ADS\]](#).
- [43] R. Khatri and R. A. Sunyaev. Forecasts for CMB μ and i -type spectral distortion constraints on the primordial power spectrum on scales $8\text{lessssim}k\text{lessssim}10^4 \text{ Mpc}^{-1}$ with the future Pixie-like experiments. *JCAP*, 6:026, June 2013. [arXiv:1303.7212](#), [\[DOI\]](#), [\[ADS\]](#).
- [44] Rishi Khatri. An alternative validation strategy for the Planck cluster catalogue and y -distortion maps. *Astron. Astrophys.*, 592:A48, 2016. [arXiv:1505.00778](#), [\[DOI\]](#).
- [45] N. Aghanim et al. Planck 2015 results. XXII. A map of the thermal Sunyaev-Zeldovich effect. *Astron. Astrophys.*, 594:A22, 2016. [arXiv:1502.01596](#), [\[DOI\]](#).
- [46] M. Remazeilles and J. Chluba. Extracting foreground-obscured μ -distortion anisotropies to constrain primordial non-Gaussianity. 2018. [arXiv:1802.10101](#).
- [47] Maximilian H. Abitbol, Jens Chluba, J. Colin Hill, and Bradley R. Johnson. Prospects for Measuring Cosmic Microwave Background Spectral Distortions in the Presence of Foregrounds. *Mon. Not. Roy. Astron. Soc.*, 471(1):1126–1140, 2017. [arXiv:1705.01534](#), [\[DOI\]](#).
- [48] J. Delabrouille et al. Exploring Cosmic Origins with CORE: Survey requirements and mission design. 2017. [arXiv:1706.04516](#).
- [49] T. Matsumura et al. LiteBIRD: Mission Overview and Focal Plane Layout. *J. Low. Temp. Phys.*, 184(3-4):824–831, 2016. [\[DOI\]](#).
- [50] H. Tashiro. CMB spectral distortions and energy release in the early universe. *Progress of Theoretical and Experimental Physics*, 2014(6):06B107, June 2014. [\[DOI\]](#), [\[ADS\]](#).
- [51] M. Kuster, G. Raffelt, and B. Beltrán, editors. *Axions*, volume 741 of *Lecture Notes in Physics*, Berlin Springer Verlag, 2008. [\[DOI\]](#), [\[ADS\]](#).
- [52] P. Sikivie. Experimental tests of the ‘invisible’ axion. *Physical Review Letters*, 51:1415–1417, October 1983. [\[DOI\]](#), [\[ADS\]](#).
- [53] G. Raffelt and L. Stodolsky. Mixing of the photon with low-mass particles. *Phys.Rev.D*, 37:1237–1249, March 1988. [\[DOI\]](#), [\[ADS\]](#).
- [54] A. A. Anselm. Experimental test for arion \leftrightarrow photon oscillations in a homogeneous constant magnetic field. *Phys.Rev.D*, 37:2001–2004, April 1988. [\[DOI\]](#), [\[ADS\]](#).
- [55] G. G. Raffelt. Particle Physics From Stars. *Annual Review of Nuclear and Particle Science*, 49:163–216, 1999. [arXiv:hep-ph/9903472](#), [\[DOI\]](#), [\[ADS\]](#).
- [56] G. G. Raffelt. *Stars as laboratories for fundamental physics : the astrophysics of neutrinos, axions, and other weakly interacting particles*. University of Chicago Press, 1996. [\[ADS\]](#).

- [57] A. Mirizzi, G. G. Raffelt, and P. D. Serpico. Photon-axion conversion as a mechanism for supernova dimming: Limits from CMB spectral distortion. *Phys.Rev.D*, 72(2):023501, July 2005. [arXiv:astro-ph/0506078](#), [DOI], [ADS].
- [58] H. Tashiro, J. Silk, and D. J. E. Marsh. Constraints on primordial magnetic fields from CMB distortions in the axiverse. *Phys.Rev.D*, 88(12):125024, December 2013. [arXiv:1308.0314](#), [DOI], [ADS].
- [59] M. S. Turner. Coherent scalar-field oscillations in an expanding universe. *Phys.Rev.D*, 28:1243–1247, September 1983. [DOI], [ADS].
- [60] W. H. Press, B. S. Ryden, and D. N. Spergel. Single mechanism for generating large-scale structure and providing dark missing matter. *Physical Review Letters*, 64:1084–1087, March 1990. [DOI], [ADS].
- [61] Sang-Jin Sin. Late-time phase transition and the galactic halo as a bose liquid. *Phys. Rev. D*, 50:3650–3654, Sep 1994. URL: <https://link.aps.org/doi/10.1103/PhysRevD.50.3650>, [DOI].
- [62] W. Hu, R. Barkana, and A. Gruzinov. Fuzzy Cold Dark Matter: The Wave Properties of Ultralight Particles. *Physical Review Letters*, 85:1158–1161, August 2000. [arXiv:astro-ph/0003365](#), [DOI], [ADS].
- [63] H.-Y. Schive, T. Chiueh, and T. Broadhurst. Cosmic structure as the quantum interference of a coherent dark wave. *Nature Physics*, 10:496–499, July 2014. [arXiv:1406.6586](#), [DOI], [ADS].
- [64] L. Hui, J. P. Ostriker, S. Tremaine, and E. Witten. Ultralight scalars as cosmological dark matter. *Phys.Rev.D*, 95(4):043541, February 2017. [arXiv:1610.08297](#), [DOI], [ADS].
- [65] L. D. Duffy and K. van Bibber. Axions as dark matter particles. *New Journal of Physics*, 11(10):105008, October 2009. [arXiv:0904.3346](#), [DOI], [ADS].
- [66] A. Ringwald. Axions and Axion-Like Particles. *ArXiv e-prints*, July 2014. [arXiv:1407.0546](#), [ADS].
- [67] D. J. E. Marsh. Axion cosmology. *Physics Reports*, 643:1–79, July 2016. [arXiv:1510.07633](#), [DOI], [ADS].
- [68] P. W. Graham, I. G. Irastorza, S. K. Lamoreaux, A. Lindner, and K. A. van Bibber. Experimental Searches for the Axion and Axion-Like Particles. *Annual Review of Nuclear and Particle Science*, 65:485–514, October 2015. [arXiv:1602.00039](#), [DOI], [ADS].
- [69] J. Ruz, J. K. Vogel, and M. J. Pivovarov. Recent Constraints on Axion-photon and Axion-electron Coupling with the CAST Experiment. *Physics Procedia*, 61:153–156, 2015. [DOI], [ADS].
- [70] N. Bastidon and I. for the ALPS collaboration. Any Light Particle Search II - Status Overview. *ArXiv e-prints*, September 2015. [arXiv:1509.02070](#), [ADS].
- [71] B. Majorovits and Javier Redondo for the MADMAX Working Group. MADMAX: A new Dark Matter Axion Search using a Dielectric Haloscope. *ArXiv e-prints*, November 2016. [arXiv:1611.04549](#), [ADS].
- [72] S. J. Asztalos et al. SQUID-Based Microwave Cavity Search for Dark-Matter Axions. *Physical Review Letters*, 104(4):041301, January 2010. [arXiv:0910.5914](#), [DOI], [ADS].
- [73] D. Budker, P. W. Graham, M. Ledbetter, S. Rajendran, and A. O. Sushkov. Proposal for a Cosmic Axion Spin Precession Experiment (CASPER). *Physical Review X*, 4(2):021030, April 2014. [arXiv:1306.6089](#), [DOI], [ADS].
- [74] T. C. Arlen, V. V. Vassilev, T. Weisgarber, S. P. Wakely, and S. Yusef Shafi. Intergalactic

- Magnetic Fields and Gamma-Ray Observations of Extreme TeV Blazars. *ApJ*, 796:18, November 2014. [arXiv:1210.2802](#), [\[DOI\]](#), [\[ADS\]](#).
- [75] K. Subramanian. The origin, evolution and signatures of primordial magnetic fields. *Reports on Progress in Physics*, 79(7):076901, July 2016. [arXiv:1504.02311](#), [\[DOI\]](#), [\[ADS\]](#).
- [76] Planck Collaboration, P. A. R. Ade, N. Aghanim, M. Arnaud, F. Arroja, M. Ashdown, J. Aumont, C. Baccigalupi, M. Ballardini, A. J. Banday, and et al. Planck 2015 results. XIX. Constraints on primordial magnetic fields. *A&A*, 594:A19, September 2016. [arXiv:1502.01594](#), [\[DOI\]](#), [\[ADS\]](#).
- [77] R. Jansson and G. R. Farrar. The Galactic Magnetic Field. *ApJL*, 761:L11, December 2012. [arXiv:1210.7820](#), [\[DOI\]](#), [\[ADS\]](#).
- [78] R. Jansson and G. R. Farrar. A New Model of the Galactic Magnetic Field. *ApJ*, 757:14, September 2012. [arXiv:1204.3662](#), [\[DOI\]](#), [\[ADS\]](#).
- [79] N. Oppermann et al. An improved map of the Galactic Faraday sky. *A&A*, 542:A93, June 2012. [arXiv:1111.6186](#), [\[DOI\]](#), [\[ADS\]](#).
- [80] Planck Collaboration, R. Adam, and et al. Planck intermediate results. XLII. Large-scale Galactic magnetic fields. *A&A*, 596:A103, December 2016. [arXiv:1601.00546](#), [\[DOI\]](#), [\[ADS\]](#).
- [81] M. I. Vysotsky, Ya. B. Zeldovich, M. Yu. Khlopov, and V. M. Chechetkin. Some Astrophysical Limitations on Axion Mass. *Pisma Zh. Eksp. Teor. Fiz.*, 27:533–536, 1978. [JETP Lett.27,502(1978)].
- [82] Z. G. Berezhiani, A. S. Sakharov, and M. Yu. Khlopov. Primordial background of cosmological axions. *Sov. J. Nucl. Phys.*, 55:1063–1071, 1992. [Yad. Fiz.55,1918(1992)].
- [83] Pankaj Jain, Sukanta Panda, and S. Sarala. Electromagnetic polarization effects due to axion photon mixing. *Phys. Rev.*, D66:085007, 2002. [arXiv:hep-ph/0206046](#), [\[DOI\]](#).
- [84] M. Millea, L. Knox, and B. D. Fields. New bounds for axions and axion-like particles with keV-GeV masses. *Phys.Rev.D*, 92(2):023010, July 2015. [arXiv:1501.04097](#), [\[DOI\]](#), [\[ADS\]](#).
- [85] Hendrik Vogel, Ranjan Laha, and Manuel Meyer. Diffuse axion-like particle searches. 2017. [arXiv:1712.01839](#).
- [86] Alessandro De Angelis, Marco Roncadelli, and Oriana Mansutti. Evidence for a new light spin-zero boson from cosmological gamma-ray propagation? *Phys. Rev. D*, 76:121301, Dec 2007. URL: <https://link.aps.org/doi/10.1103/PhysRevD.76.121301>, [\[DOI\]](#).
- [87] Alessandro De Angelis, Giorgio Galanti, and Marco Roncadelli. Relevance of axionlike particles for very-high-energy astrophysics. *Phys. Rev. D*, 84:105030, Nov 2011. URL: <https://link.aps.org/doi/10.1103/PhysRevD.84.105030>, [\[DOI\]](#).
- [88] Fabrizio Tavecchio, Marco Roncadelli, Giorgio Galanti, and Giacomo Bonnoli. Evidence for an axion-like particle from pks 1222+216? *Phys. Rev. D*, 86:085036, Oct 2012. URL: <https://link.aps.org/doi/10.1103/PhysRevD.86.085036>, [\[DOI\]](#).
- [89] Martin Schlederer and GÅ¼nter Sigl. Constraining ALP-photon coupling using galaxy clusters. *JCAP*, 1601(01):038, 2016. [arXiv:1507.02855](#), [\[DOI\]](#).
- [90] Guido D’Amico and Nemanja Kaloper. Anisotropies in nonthermal distortions of cosmic light from photon-axion conversion. *Phys. Rev.*, D91(8):085015, 2015. [arXiv:1501.01642](#), [\[DOI\]](#).
- [91] M. Born and E. Wolf. *Principles of optics*. Cambridge University Press, 1999.
- [92] A. Mirizzi, J. Redondo, and G. Sigl. Microwave background constraints on mixing of photons with hidden photons. *JCAP*, 3:026, March 2009. [arXiv:0901.0014](#), [\[DOI\]](#), [\[ADS\]](#).
- [93] Y. Grossman, S. Roy, and J. Zupan. Effects of initial axion production and photon-axion oscillation on type Ia supernova dimming [rapid communication]. *Physics Letters B*, 543:23–28, September 2002. [arXiv:hep-ph/0204216](#), [\[DOI\]](#), [\[ADS\]](#).

- [94] S. P. Mikheyev and A. Y. Smirnov. Resonance enhancement of oscillations in matter and solar neutrino spectroscopy. *Yadernaya Fizika*, 42:1441–1448, 1985. [ADS].
- [95] L. Wolfenstein. Neutrino oscillations in matter. *Phys.Rev.D*, 17:2369–2374, May 1978. [DOI], [ADS].
- [96] H. A. Bethe. Possible explanation of the solar-neutrino puzzle. *Physical Review Letters*, 56:1305–1308, March 1986. [DOI], [ADS].
- [97] L. D. Landau. To the theory of energy transmission in collisions. II. *Phys. Zs. Sowjet.*, 2, p. 46, 1932 (*English and German*), 2:46, December 1932. [ADS].
- [98] C. Zener. Non-Adiabatic Crossing of Energy Levels. *Proceedings of the Royal Society of London Series A*, 137:696–702, September 1932. [DOI], [ADS].
- [99] E. C. G. Stueckelberg. Theorie der unelastischen Stoesse zwischen Atomen. *Helvetica Physica Acta*, 5:369, 1932.
- [100] T. K. Kuo and J. Pantaleone. Neutrino oscillations in matter. *Reviews of Modern Physics*, 61:937–980, October 1989. [DOI], [ADS].
- [101] J. Lesgourgues. The Cosmic Linear Anisotropy Solving System (CLASS) I: Overview. *ArXiv e-prints*, April 2011. [arXiv:1104.2932](https://arxiv.org/abs/1104.2932), [ADS].
- [102] Y. Ali-Haïmoud and C. M. Hirata. Ultrafast effective multilevel atom method for primordial hydrogen recombination. *Phys.Rev.D*, 82(6):063521, September 2010. [arXiv:1006.1355](https://arxiv.org/abs/1006.1355), [DOI], [ADS].
- [103] Y. Ali-Haïmoud and C. M. Hirata. HyRec: A fast and highly accurate primordial hydrogen and helium recombination code. *Phys.Rev.D*, 83(4):043513, February 2011. [arXiv:1011.3758](https://arxiv.org/abs/1011.3758), [DOI], [ADS].
- [104] J. Chluba and R. M. Thomas. Towards a complete treatment of the cosmological recombination problem. *MNRAS*, 412:748–764, April 2011. [arXiv:1010.3631](https://arxiv.org/abs/1010.3631), [DOI], [ADS].
- [105] D. P. Cox and R. J. Reynolds. The local interstellar medium. *ARA&A*, 25:303–344, 1987. [DOI], [ADS].
- [106] P. C. Frisch, S. Redfield, and J. D. Slavin. The Interstellar Medium Surrounding the Sun. *ARA&A*, 49:237–279, September 2011. [DOI], [ADS].
- [107] S. L. Snowden. Pressure Equilibrium between the Local Interstellar Clouds and the Local Hot Bubble. *ApJL*, 791:L14, August 2014. [DOI], [ADS].
- [108] A. Mirizzi, J. Redondo, and G. Sigl. Constraining resonant photon-axion conversions in the early universe. *JCAP*, 8:001, August 2009. [arXiv:0905.4865](https://arxiv.org/abs/0905.4865), [DOI], [ADS].
- [109] L. Stodolsky. Treatment of neutrino oscillations in a thermal environment. *Phys.Rev.D*, 36:2273–2277, October 1987. [DOI], [ADS].
- [110] J. Jaeckel, J. Redondo, and A. Ringwald. Signatures of a Hidden Cosmic Microwave Background. *Physical Review Letters*, 101(13):131801, September 2008. [arXiv:0804.4157](https://arxiv.org/abs/0804.4157), [DOI], [ADS].
- [111] G. L. Fogli, E. Lisi, A. Mirizzi, and D. Montanino. Analysis of energy and time dependence of supernova shock effects on neutrino crossing probabilities. *Phys.Rev.D*, 68(3):033005, August 2003. [arXiv:hep-ph/0304056](https://arxiv.org/abs/hep-ph/0304056), [DOI], [ADS].
- [112] Y. Kayanuma. Phase coherence and nonadiabatic transition at a level crossing in a periodically driven two-level system. *Phys.Rev.B*, 47:9940–9943, April 1993. [DOI], [ADS].
- [113] B. Dasgupta and A. Dighe. Phase effects in neutrino conversions during a supernova shock wave. *Phys.Rev.D*, 75(9):093002, May 2007. [arXiv:hep-ph/0510219](https://arxiv.org/abs/hep-ph/0510219), [DOI], [ADS].

- [114] K. M. Gorski, Eric Hivon, A. J. Banday, B. D. Wandelt, F. K. Hansen, M. Reinecke, and M. Bartelman. HEALPix - A Framework for high resolution discretization, and fast analysis of data distributed on the sphere. *Astrophys. J.*, 622:759–771, 2005. [arXiv:astro-ph/0409513](#), [DOI].
- [115] L. Guzzo. Is the universe homogeneous? (On large scales). *New Astronomy*, 2:517–532, December 1997. [arXiv:astro-ph/9711206](#), [DOI], [ADS].
- [116] J. Pan and P. Coles. Large-scale cosmic homogeneity from a multifractal analysis of the PSCz catalogue. *MNRAS*, 318:L51–L54, November 2000. [arXiv:astro-ph/0008240](#), [DOI], [ADS].
- [117] J. Yadav, S. Bharadwaj, B. Pandey, and T. R. Seshadri. Testing homogeneity on large scales in the Sloan Digital Sky Survey Data Release One. *MNRAS*, 364:601–606, December 2005. [arXiv:astro-ph/0504315](#), [DOI], [ADS].
- [118] D. W. Hogg, D. J. Eisenstein, M. R. Blanton, N. A. Bahcall, J. Brinkmann, J. E. Gunn, and D. P. Schneider. Cosmic Homogeneity Demonstrated with Luminous Red Galaxies. *ApJ*, 624:54–58, May 2005. [arXiv:astro-ph/0411197](#), [DOI], [ADS].
- [119] M. I. Scrimgeour et al. The WiggleZ Dark Energy Survey: the transition to large-scale cosmic homogeneity. *MNRAS*, 425:116–134, September 2012. [arXiv:1205.6812](#), [DOI], [ADS].
- [120] S. Sarkar and B. Pandey. An information theory based search for homogeneity on the largest accessible scale. *MNRAS*, 463:L12–L16, November 2016. [arXiv:1607.06194](#), [DOI], [ADS].
- [121] M. J. Miller and J. N. Bregman. The Structure of the Milky Way’s Hot Gas Halo. *ApJ*, 770:118, June 2013. [arXiv:1305.2430](#), [DOI], [ADS].
- [122] J. M. Cordes and T. J. W. Lazio. NE2001.I. A New Model for the Galactic Distribution of Free Electrons and its Fluctuations. *ArXiv Astrophysics e-prints*, July 2002. [arXiv:astro-ph/0207156](#), [ADS].
- [123] V. J. Martinez and P. Coles. Correlations and scaling in the QDOT redshift survey. *ApJ*, 437:550–555, December 1994. [DOI], [ADS].
- [124] S. Borgani. Scaling in the Universe. *Physics Reports*, 251:1–152, January 1995. [arXiv:astro-ph/9404054](#), [DOI], [ADS].
- [125] A. Cappi, C. Benoist, L. N. da Costa, and S. Maurogordato. Is the Universe a fractal? Results from the Southern Sky Redshift Survey 2. *A&A*, 335:779–788, July 1998. [ADS].
- [126] A. Zitrin and N. Brosch. The NGC 672 and 784 galaxy groups: evidence for galaxy formation and growth along a nearby dark matter filament. *MNRAS*, 390:408–420, October 2008. [arXiv:0808.1789](#), [DOI], [ADS].
- [127] R. B. Tully, E. J. Shaya, I. D. Karachentsev, H. M. Courtois, D. D. Kocevski, L. Rizzi, and A. Peel. Our Peculiar Motion Away from the Local Void. *ApJ*, 676:184–205, March 2008. [arXiv:0705.4139](#), [DOI], [ADS].
- [128] B. M. Gaensler, G. J. Madsen, S. Chatterjee, and S. A. Mao. The Vertical Structure of Warm Ionised Gas in the Milky Way. *Publications of the Astronomical Society of Australia*, 25:184–200, November 2008. [arXiv:0808.2550](#), [DOI], [ADS].
- [129] K. Beuermann, G. Kanbach, and E. M. Berkhuijsen. Radio structure of the Galaxy - Thick disk and thin disk at 408 MHz. *A&A*, 153:17–34, December 1985. [ADS].
- [130] X. H. Sun, W. Reich, A. Waelkens, and T. A. Enßlin. Radio observational constraints on Galactic 3D-emission models. *A&A*, 477:573–592, January 2008. [arXiv:0711.1572](#), [DOI], [ADS].
- [131] M. Haverkorn, J. C. Brown, B. M. Gaensler, and N. M. McClure-Griffiths. The Outer Scale of Turbulence in the Magnetoionized Galactic Interstellar Medium. *ApJ*, 680:362–370, June 2008. [arXiv:0802.2740](#), [DOI], [ADS].

- [132] J. L. Han, W. van Straten, T. J. W. Lazio, A. Deller, C. Sobey, J. Xu, D. Schnitzeler, H. Imai, S. Chatterjee, J.-P. Macquart, M. Kramer, and J. M. Cordes. Three-dimensional Tomography of the Galactic and Extragalactic Magnetoionic Medium with the SKA. *Advancing Astrophysics with the Square Kilometre Array (AASKA14)*, page 41, April 2015. [arXiv:1412.8749](#), [ADS].
- [133] J. W. Armstrong, B. J. Rickett, and S. R. Spangler. Electron density power spectrum in the local interstellar medium. *ApJ*, 443:209–221, April 1995. [DOI], [ADS].
- [134] M. Tegmark, A. N. Taylor, and A. F. Heavens. Karhunen-Loève Eigenvalue Problems in Cosmology: How Should We Tackle Large Data Sets? *ApJ*, 480:22–35, May 1997. [arXiv:astro-ph/9603021](#), [DOI], [ADS].
- [135] Planck Collaboration, R. Adam, P. A. R. Ade, N. Aghanim, M. I. R. Alves, M. Arnaud, M. Ashdown, J. Aumont, C. Baccigalupi, A. J. Banday, and et al. Planck 2015 results. X. Diffuse component separation: Foreground maps. *A&A*, 594:A10, September 2016. [arXiv:1502.01588](#), [DOI], [ADS].
- [136] P. Platania, M. Bensadoun, M. Bersanelli, G. De Amici, A. Kogut, S. Levin, D. Maino, and G. F. Smoot. A Determination of the Spectral Index of Galactic Synchrotron Emission in the 1-10 GHz Range. *ApJ*, 505:473–483, October 1998. [arXiv:astro-ph/9707252](#), [DOI], [ADS].
- [137] M. O. Irfan, C. Dickinson, R. D. Davies, C. Copley, R. J. Davis, P. G. Ferreira, C. M. Holler, J. L. Jonas, M. E. Jones, O. G. King, J. P. Leahy, J. Leech, E. M. Leitch, S. J. C. Muchovej, T. J. Pearson, M. W. Peel, A. C. S. Readhead, M. A. Stevenson, D. Sutton, A. C. Taylor, and J. Zuntz. C-Band All-Sky Survey: a first look at the Galaxy. *MNRAS*, 448:3572–3586, April 2015. [arXiv:1501.06069](#), [DOI], [ADS].
- [138] A. Payez, C. Evoli, T. Fischer, M. Giannotti, A. Mirizzi, and A. Ringwald. Revisiting the SN1987A gamma-ray limit on ultralight axion-like particles. *JCAP*, 2:006, February 2015. [arXiv:1410.3747](#), [DOI], [ADS].
- [139] Joseph P. Conlon, M. C. David Marsh, and Andrew J. Powell. Galaxy cluster thermal x-ray spectra constrain axionlike particles. *Phys. Rev.*, D93(12):123526, 2016. [arXiv:1509.06748](#), [DOI].